TECHNICAL ARTICLE

Effect of Zinc and Bio-Glass Addition on Mechanical Properties and Corrosion Behavior of Magnesium-Based Composites for Orthopedic Application: A Preliminary Study

K.V. Sandeep Moudgalya, Prithivirajan Sekar ⓘ, H. Suresh Hebbar, and M.R. Rahman

Magnesium is extensively researched as a biodegradable implant material. However, achieving a combination of biomechanical properties viz., controlled degradation, bio-transformability and osteoconductivity is highly challenging. Indeed, bio-composites developed by reinforcing bio-ceramics with metals are gaining research interest. In this current work, the suitability of a bio-composite developed by reinforcing 5, 10 and 15% of bioglass (BG) in Mg and Mg-3 wt.% Zn metal matrix is investigated. The bio-composites containing Mg, Mg-BG and Mg-Zn-BG are processed by vacuum sintering and tested for important mechanical and corrosion properties. Particle size analysis revealed that magnesium exhibited a larger mean particle size while zinc evinced the lowest average particle size. The density-porosity analysis showed that porosity was found to increase linearly with the addition of BG. In contrast, the compressive strength of Mg-BG and Mg-Zn-BG composites increased up to 10 wt.% BG and decreased drastically for 15 wt.% BG reinforcement. The addition of Zn and BG significantly enhanced the Vickers hardness, showing an increasing trend with the increase in BG reinforcement content. Immersion corrosion study in phosphate buffered saline revealed that 10 wt.% BG reinforced composite exhibited the least corrosion rate. Thus, composites developed by reinforcing BG in Mg-3Zn metal matrix showed enhanced mechanical and corrosion properties in the physiological environment. The possible corrosion mechanism of Mg, Mg-Zn and Mg-Zn-BG composites is also proposed and compared.

1. Introduction

Self-healing nature of bone is a blessing to the human race. Bone remodeling is a lively process in which osteoblasts promote new bone formation and osteoclasts perform resorption of old bones. However, there is a critical bone defect size beyond which the human body cannot heal completely by itself. These relatively large scale bone defects often occur as a result of a wide variety of cases, especially trauma and

K.V. Sandeep Moudgalya and **H. Suresh Hebbar**, Department of Mechanical Engineering, National Institute of Technology Karnataka, Surathkal, Srinivasanagar, Mangalore, Karnataka 575025, India; **Prithivirajan Sekar**, Department of Production Engineering, PSG College of Technology, Avinashi Road, Peelamedu, Coimbatore, Tamilnadu 641004, India; and **M.R. Rahman**, Department of Metallurgical and Materials Engineering, National Institute of Technology Karnataka, Surathkal, Srinivasanagar, Mangalore, Karnataka 575025, India. Contact e-mail: sekarprithiviraj@gmail.com.

osteonecrosis. To heal such large scale bone defects insertion of implants become mandatory (Ref 1, 2). Orthopedic implant materials are one of the most important biomedical materials. Among potential materials on which the research is in progress, Magnesium-based biomaterials are found to be interesting. This is because of its excellent biocompatibility, biodegradability, elastic modulus and density which are close to that of human bone. However, the major challenge in its use as a biomaterial is its high degradation rate (Ref 3). Alloying, grain refinement and use of coatings have been extensively used to increase the corrosion resistance of Mg. However, the addition of toxic elements such as Aluminum (Al) and Rare Earths (RE) are not recommended. The additive elements included in Mg system also from galvanic cells which leads to deterioration in corrosion resistance. In contrast, the coating assists corrosion resistance only in the earlier stages of degradation (Ref 4). Hence, the use of ceramics as reinforcements in Mg has emerged as a new strategy to improve mechanical properties as well as to combat corrosion. Alumina, Titania, zirconia, bioactive glasses, calcium phosphate-based ceramics like hydroxyapatite (HAp), tri-calcium phosphate (TCP) are some of the majorly researched ceramic biomaterials. Ceramics are known for their good biocompatibility, good corrosion and wear resistance and high compressive strength (Ref 5). One of the initial attempts of developing magnesium-based composites for the biomedical application was explored by Witte and co-workers. Hydroxyapatite (HAp) reinforced in the AZ91D alloy exhibited better corrosion behavior based on the immersion test

carried out in Dulbecco's modified eagle medium (Ref 6). Jaiswal et al. developed Mg 3 wt.% Zn metal matrix reinforced with hydroxyapatite bioactive ceramic. The addition of 5 wt.% hydroxyapatite improved the corrosion resistance and mechanical strength significantly with good osteo-compatibility (Ref 7). The mechanical, corrosion and biological properties of BG reinforced Magnesium composites were investigated. Mg-BG composite with 10 wt.% BG was found to exhibit the best mechanical and biological properties (Ref 8). Kowalski et al. reported the influence of BG on magnesium metal matrix with 4 wt.% Yttrium, 5.5 wt.% Dysprosium, 0.5 wt.% Zirconium. Further fluoride treatment was carried out as well. Enhanced mechanical properties were observed for the composites due to the ultrafine grain structure (Ref 9). BG reinforced magnesium metal matrix composite was processed through spark plasma sintering and hot press sintering process. Higher corrosion resistance was reported for Mg-10 wt.% BG reinforced composite after immersion in PBS medium (Ref 10, 11). The addition of zinc up to 3 wt.% was found to enhance tensile strength, % elongation and corrosion resistance. Beyond 3 wt.% Zinc addition, corrosion resistance and ductility were reduced due to the formation of crack initiation sites. So, researchers concluded that Zn with 3 wt.% is the most optimal choice for orthopedic applications (Ref 12, 13). Despite intense research on Mg as a biodegradable implant over the years, making them commercially available in the market is still challenging (Ref 14). Therefore, an effort has been made in the present study to produce Mg composites with Zinc and BG addition. Mg possesses excellent biocompatibility and elastic modulus comparable to human bone. But, it exhibits relatively lower osteoconductivity than BG. In contrast, BG acts like a partial coating and possess extraordinary osteoconductivity that assists active bone regeneration in vivo. However, its brittle nature remains a hindrance in clinical applications. The combination of Mg, Zn and BG is expected to exhibit controllable biodegradation, mechanical properties comparable to cortical bone and outstanding osteoconductivity. Therefore, in the present study, BG is reinforced in Mg and Mg-3 Zn wt.% metal matrix to function as a potential bone fixative implant. Also, the mechanical properties and corrosion behavior of Mg, Mg-BG and Mg-Zn-BG composites are studied. From the accessible literature, bio-ceramic reinforced with metals has dwelt less in the field of biomaterials research. Hence, in this research work, a bio-composite developed by reinforcing a bio-ceramic with metals for bone fixative application is explored.

2. Experimental Procedure

2.1 Raw Materials and Sample Preparation

The materials used in the preparation of the metal matrix composite consisted of magnesium (Mg) and zinc (Zn), forming a metal matrix, while bioglass 45S5 (BG) was added as reinforcement material. Bioglass 45S5 with a constituent composition of 45% Silica (SiO_2), 24.5% Calcium Oxide (CaO), 24.5% Sodium Oxide (Na_2O) and 6% Phosphorous Oxide (P_2O_5) was used. 99% pure magnesium metal powder was procured from Neeraj industries, Rohtak, Haryana, India. 95% pure zinc metal powder was procured from Loba Chemie private limited, Mumbai, India and Bioglass 45S5 fine powders was procured from XL Sci-Tech, Inc, Richland, Washington,

USA. Compositions of the composites under study are shown in Table 1. Weighed proportions of Mg, Zn and BG were homogenously mixed using an ultrasonic probe sonicator (Probe Sonicator PKS 250FL), with acetone as the sonicating medium. The sonication was carried out at a sonication frequency of 20 kHz for 20 min with intermittent running cycles. The sonicated powders were then dried in a vacuum oven at 60 °C for an hour to ensure no trace of acetone is leftover. Compaction of sonicated powders was carried out to prepare two sets of samples (i) cylindrical samples of size 10 mm diameter and 15 mm height and (ii) cuboidal samples with a square cross-section of 15 mm and 5 mm thickness. The cylindrical samples were used for mechanical characterization while cuboidal samples were used for all the other studies including those related to corrosion analysis. The compaction was carried out in a universal testing machine with a compaction load of 600 MPa and a holding time of 5 min. The compaction load and holding time are maintained constant for all the Mg, Mg-Zn and Mg-Zn-BG samples. The green compacts were then subjected to vacuum sintering in a high-temperature vacuum furnace. The sintering was carried out in a vacuum controlled environment with vacuum pressure maintained at 0.05 mBar. The heating rate, sintering temperature and holding time were set at 15 °C/min, 550 °C and 2 h, respectively, followed by furnace cooling up to room temperature in controlled vacuum conditions. Indeed, the microstructure, mechanical properties and corrosion behavior of sintered Mg, Mg-Zn and Mg-Zn-BG samples were evaluated.

2.2 Powder Characterization

Before carrying out the sonication process, the raw material powders were analyzed using scanning electron microscope (SEM) micrographs, x-ray diffraction (XRD) and particle size characterization techniques. SEM micrographs of raw material powders and sonicated powders were analyzed using JEOL JSM-6380LA scanning electron microscope. Particle size analysis was carried out using electron microscopy technique, as per the ASTM standard guide for powder particle size analysis—ASTM E2651-19. All the discrete and individual particles noticeable to the best extent in the microscopic image were measured using Image J software.

JEOL x-ray diffractometer was used for the analysis of the raw material powders, sonicated powders and sintered composites. Copper Kα radiation with a wavelength of 1.54056 Å, 2Theta range of 20°-80°, a step size of 0.02 and a scan rate of 2°/min was used for acquiring diffraction peaks. Phase identification was carried out by matching the peaks with Joint committee on powder diffraction standards (JCPDS) files.

2.3 Microstructural Characterization

Optical microscopic imaging was done using ZEISS Axiolab microscope with Axio vision software for image capture. Electron microscopic imaging of sintered composites was also carried using ZEISS sigma Field emission scanning electron microscope (FESEM). Energy dispersive spectroscopy (EDS) characterization and corroded surface morphology were studied using Hitachi SU 3500N SEM. Prior microstructural observations Mg, Mg-Zn and Mg-Zn-BG samples were ground up to 2000 grid size silicon carbide (SiC) papers followed by velvet cloth polish with 0.5 μm and 0.25 μm diamond paste. Acetic glycol was used as an etchant for revealing grain boundaries in

Table 1 Sample codes corresponding to the compositions of composites

Sample code	Composition	Sample code	Composition
M-0-0	Pure Mg (100 wt.% Mg)	M-3-0	97 wt.% Mg-3 wt.% Zn
M-0-5	95 wt.% Mg-5 wt.% BG	M-3-5	92 wt.% Mg-3 wt.% Zn-5 wt.% BG
M-0-10	90 wt.% Mg-10 wt.% BG	M-3-10	87 wt.% Mg-3 wt.% Zn-10 wt.% BG
M-0-15	85 wt.% Mg-15 wt.% BG	M-3-15	82 wt.% Mg-3 wt.% Zn-15 wt.% BG

the sintered Mg composites. Grain size analysis was done as per ASTM E1382-97 standard using Image J software.

2.4 Mechanical Characterization

Theoretical density was carried out based on the law of mixtures, while Archimedes principle was employed to carry out the density measurements of the sintered composites as per ASTM–B962-17 standard. Porosity ratio (PR) was calculated based on the equation PR = (1 − (Measured density/Theoretical density)). At least 3 repetitions for each composition of the composites were carried out. The compression tests were carried out on each of the eight compositions of the sintered composites using Zwick Roell UTM. ASTM E9-09 standard was followed for carrying out the tests with a loading rate of 0.5 mm/min and a length to diameter (L/D) ratio of 1.5. At least 3 trials were done for each composition. The hardness test was carried out in Vickers 402 MVD Francis Kein instrument. The test was carried out through a diamond indenter of 138° angle. A load of 100 g and a dwell time of 10 s was considered for the test. The Hardness test was carried out with at least 9 indentations on each composition.

2.5 Corrosion Study

Corrosion tests were carried out using phosphate buffered saline (PBS) as corrosion medium. PBS salt having an ingredient concentration of 0.795 g/l of anhydrous disodium hydrogen phosphate, 0.144 g/l potassium dihydrogen phosphate and 9 g/l sodium chloride was procured from Himedia. The pH of the medium was adjusted to 7.4 using 1N hydrochloric acid and 1N sodium hydroxide, to simulate the pH of the physiological environment.

2.5.1 Electrochemical Characterization. Electrochemical corrosion tests were carried out using Gill AC-1684 electrochemical corrosion analyzer. Graphite was used as an auxiliary electrode while a saturated calomel electrode was used as the reference electrode. A cuboidal sample with 1 cm^2 of exposed area was used as the working electrode with PBS as corrosion medium. Potentiodynamic polarization tests were carried out over a range of − 200 mV to + 200 mV with a scan rate of 2 mV/sec. Electrochemical impedance spectroscopy was carried out over a frequency range of 10 kHz to 10 mHz. The corrosion rate was calculated based on the Tafel extrapolation technique, using the equation, corrosion rate = 22.85 * corrosion current density (mA/cm^2) (Ref 15, 16).

2.5.2 Immersion Corrosion. The cuboidal shaped composites were used for carrying out the immersion corrosion test in PBS medium. The sample length, breadth and height were 10 ± 2 mm, 6 ± 2 mm and 3 ± 1 mm, respectively. The ratio of the volume of the corrosion medium to the exposed surface area of the sample was above 20 ml/cm^2, as per ASTM G31-72 for immersion corrosion study. All the sides of the samples were grinded up to 2000 grid size SiC abrasive paper followed by velvet cloth polish. The samples were cleaned using ethanol and then dried before immersing in the corrosion medium. The temperature of the solution was maintained at 37 °C in a vacuum incubator. Three immersion periods, 24 h, 48 h and 72 h, were considered for testing. The mass of each sample was measured before and after immersion in the corrosion medium to quantify the degradation. Prior to measuring the mass of the sample after immersion, the corroded samples were washed 180 g/l chromic acid followed by ethanol. The mass of the corroded samples was measured after keeping the sample in a vacuum desiccator for 24 h, post drying of the cleaned sample. The corrosion rate was determined based on the equation obtained as per ASTM G31-72 standard.

$$CR = \frac{8.76 \times 10^4 \times \Delta m}{A \times t \times \rho}$$

where CR = Corrosion rate in mm/year, Δm = Difference in mass before and after immersion in g, A = Surface area of the sample in contact with corrosion medium in cm^2, t = Immersion time in hrs, ρ = Density of the sample in g/cm^3.

2.6 Statistical Analysis

Statistical Analysis was carried out based on Student's t-test method in which $p < 0.05$ was considered to be statistically significant (represented by * symbol). All the experimental values were expressed as mean ± standard deviation.

3. Results and Discussion

3.1 Microscopic Observation and XRD Patterns of Raw Materials

Prior to the preparation of metal matrix composite, raw material powders were analyzed to know the particle shape and size. Figure 1(a)-(c) shows microscopic images of pure magnesium, pure zinc and 45S5 BG powder, respectively. Pure magnesium metal powders were observed to be of irregular flakes and rod-like particles. Pure zinc metal powders were majorly spherical shaped and rounded particles. The 45S5 BG powders were found to be composed of angularly shaped particles with low sphericity. XRD patterns of pure Magnesium, Zinc and BG powders is shown in Fig. 1(d)-(f), respectively. The peaks generated for pure magnesium were matched with corresponding JCPDS file for magnesium powders. Mg was the only major phase found. Zn was the majorly observed phase in pure Zn powder with a minor ZnO
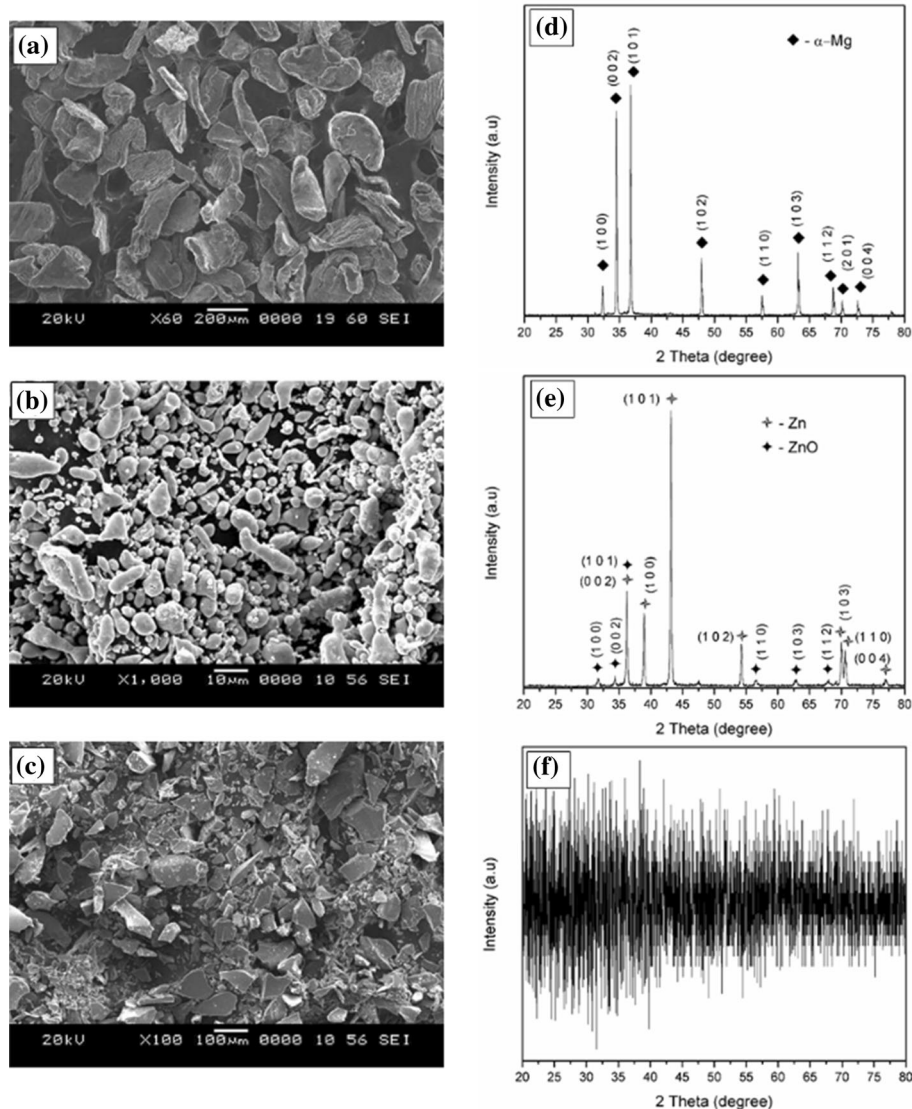
Fig. 1 SEM micrographs of as received (a) Mg, (b) Zn and (c) BG powders; XRD pattern of as received (d) Mg, (e) Zn and (f) BG powders

phase also being detected. 45S5 BG powder was found to be amorphous, while no crystal peaks were observed.

3.2 Particle Size Analysis of Raw Materials

Particle size analysis is essential to know the distribution of the powders which impacts the compaction of powders and hence the product properties. Powder constituents with different particle size ranges are desirable for better densification. In this work, particle size analysis is carried out by using electron microscopy technique. Particle size distribution of pure magnesium, pure zinc powder and 45S5 BG is shown in Fig. 2(a)-(c) and the corresponding mean values are represented in Fig. 2(d). Pure magnesium powders were predominantly clustered around 151-200 μm range, with a mean at 183.72 μm. 45S5 BG powders were found to be spread in a wider range but predominantly focused around 41-60 μm range, with a mean at 62.59 μm. Pure zinc powders were majorly found in 4-6 μm range, with an average of 5.74 μm. Interestingly, the particle size distribution of all the raw material

powders followed a transitional behavior, with frequency topped at some mid-range while falling low on either side. Most importantly, particle sizes of zinc and reinforcement, i.e., BG are significantly lesser than the particle size of magnesium. This is also clearly visible in SEM micrographs (refer to Fig. 1) of raw material powders. The smaller size of Zinc and BG reinforcements assists in accommodating the interstices of the Mg matrix, leading to better compaction.

3.3 SEM and XRD Characterization of Sonicated Powders

Figure 3(a)-(e) depicts the SEM micrographs of sonicated powders. In M-0-0 sample, pure Mg powders were seen in the form of irregular flakes and rod-like particles. With the addition of 3 wt.% Zinc, spherical and round-shaped Zinc particles coexist along with pure Mg powders evident from Fig. 3(b). On the contrary, when both Zinc and BG powders are added, Zinc and BG powder particles coexisted with Mg powder particles evident from Fig. 3(c) (d) and (e). Zinc powder particles were observed with very fine dots dispersed uniformly in the matrix, in all compositions
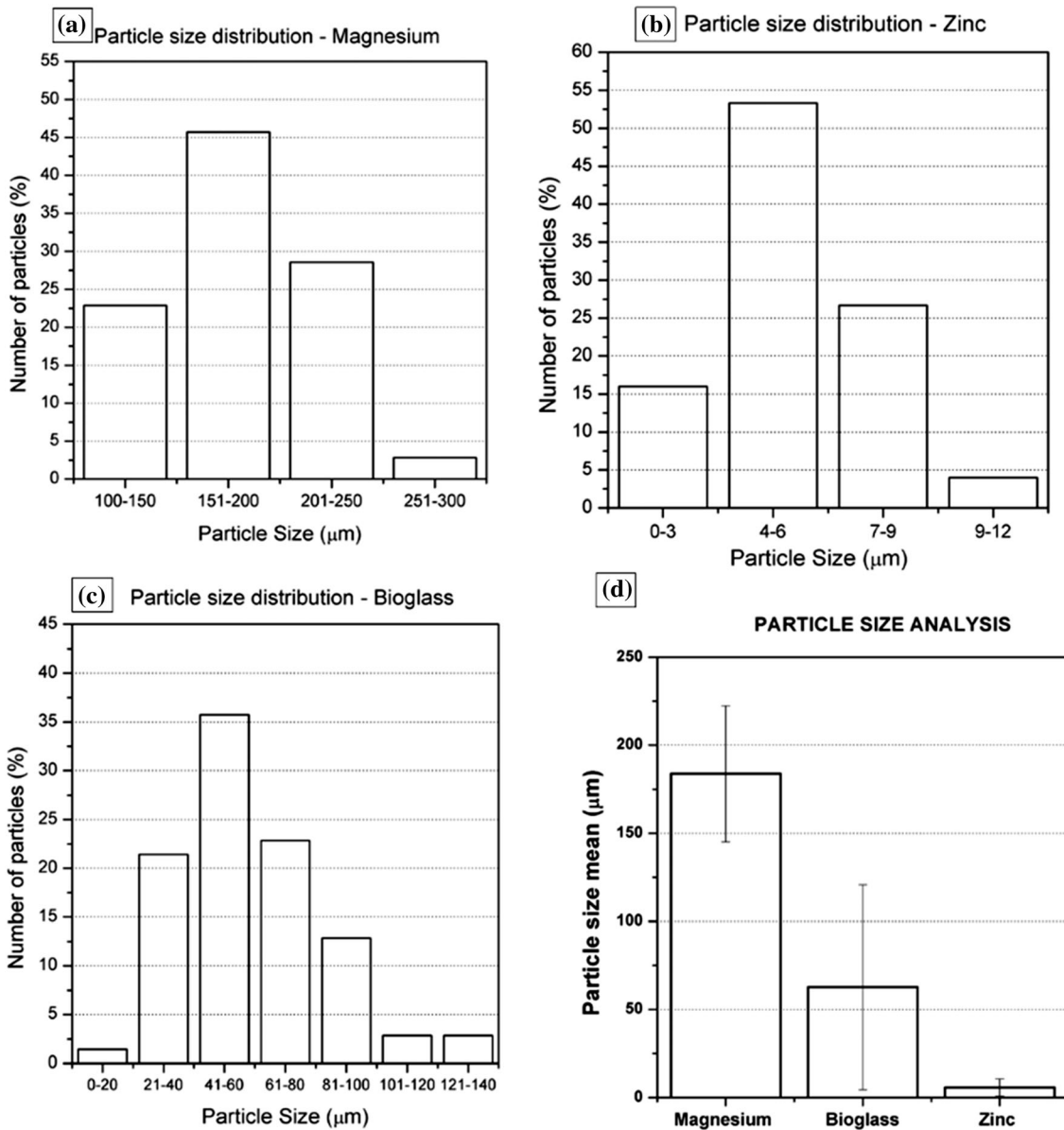
Fig. 2 Particle size distribution of as received (a) Mg, (b) Zn and (c) BG powders; (d) Mean particle size of as received Mg, Zn and BG powders

excluding M-0-0. BG reinforcement was less noticeable in M-3-5 composition as observed from Fig. 3(c). This is because of the relatively lower 5 wt.% of the BG reinforcement added in Mg matrix. However, BG reinforcements were predominantly distinguishable for M-3-10 and M-3-15, observed from Fig. 3(d) and (e), respectively. It is noteworthy to mention that compared to M-3-10 sample relatively better compaction was achieved in M-3-15 sample. This compaction phenomenon of sonicated samples is in line with SEM micrographs (refer Fig. 1) and particles size of individual Mg, Zn and BG powders (refer Fig. 2). Indeed, XRD analysis was also carried out on sonicated powders of all compositions and is represented in Supplementary Fig. S1. XRD analysis assisted in finding out whether the sonication caused the formation of any possible phases. Magnesium was the only metallic phase observed predominantly in all the compositions. Hence, it is confirmed that no specific phase formation between the constituent elements was observed.

3.4 Microscopic Imaging of Mg, Mg-BG and Mg-Zn-BG Sintered Composites

Microstructural features observed using OM are represented in Fig. 4. The grains and grain boundaries were noticeable for all the compositions. The microstructure of both M-0-0 and M-3-0 was observed to be similar but the core matrix phase was different. Mg was the only major phase in M-0-0, while MgZn was the predominant matrix phase for M-3-0. BG was differentiable in OM with dark irregular shaped grain particles in all the BG reinforced composites. The number of ceramic grains observed in BG reinforced composites viz., M-0-5, M-0-10, M-0-15, M-3-5, M-3-10 and M-3-15 was found to be increasing with percentage reinforcements. However, the grain size of Mg-Zn-BG composites viz., M-3-5, M-3-10 and M-3-15 were relatively lower than the corresponding Mg-BG composites viz., M-0-5, M-0-10 and M-0-15. Recent research claimed
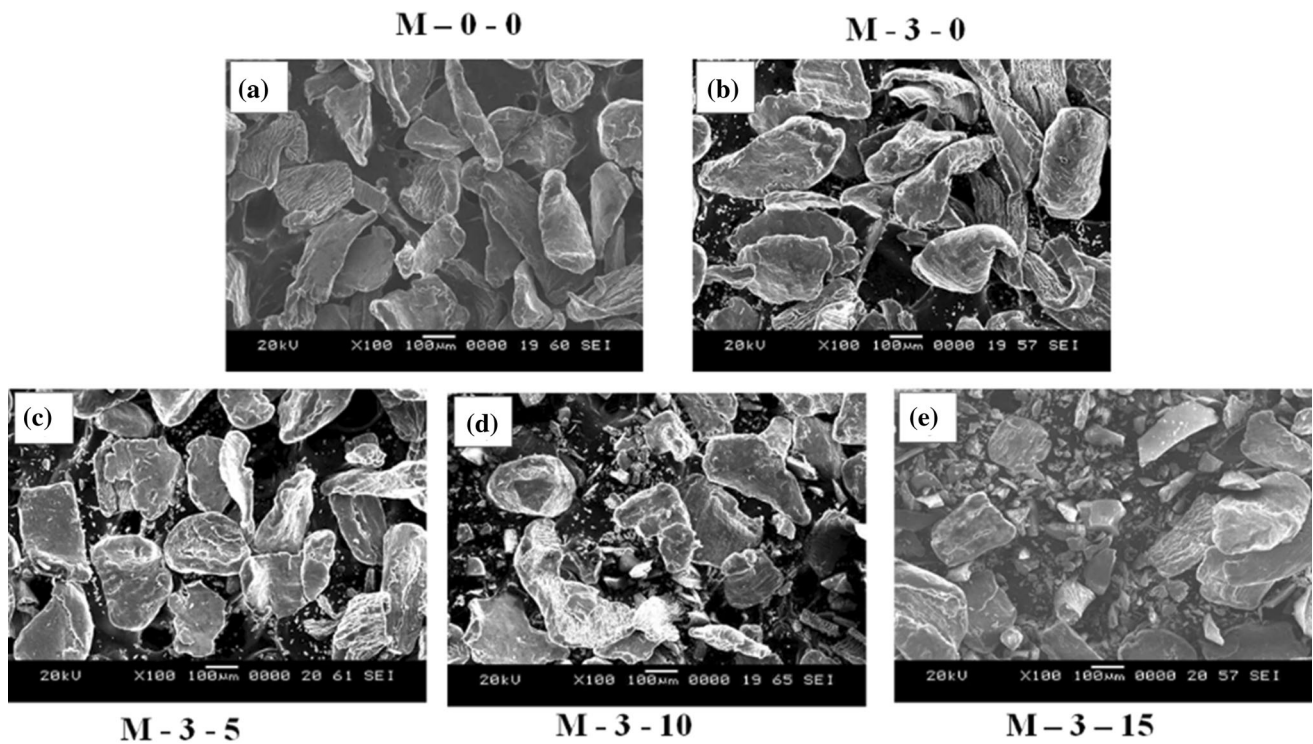
Fig. 3 SEM micrographs of sonicated powders (a) M-0-0 (b) M-3-0 (c) M-3-5 (d) M-3-10 (e) M-3-15

that the grain characters influenced the mechanical properties and corrosion behavior of Magnesium. Hence, the grain characteristics of the Mg composites with varying BG proportion with and without Zinc addition is analyzed. The mean linear intercept and grain size of Mg-BG and Mg-Zn-BG composites are depicted in Fig. 5(a)-(b), respectively. The mean linear intercepts of Mg-Zn-BG composites were relatively lower than the Mg-BG composites. In addition, the grain area of Mg composites decreased with 3% Zn addition in the Mg matrix. Interestingly, the statistical study revealed that the decrease in grain area was statistically significant $p = 0.048$ and $p = 0.016$ in case of 5 % and 10 % BG reinforcements, respectively. The sintered Mg-Zn-BG composites were observed by using FESEM to get further insights into microstructural features. The FESEM micrographs of Mg and Mg-Zn-BG composites were represented in Fig. 6(a)-(e). The microstructural features of M-0-0 and M-3-0 samples were comparable. The addition of 3 wt.% Zinc a exhibited relative decrease in grain size as observed from Fig. 6(b). In contrast, with the addition of BG reinforcements in Mg-3 wt.% Zinc matrix, two important features were observed (i) agglomeration of BG predominantly along the grain boundaries (ii) formation of micropores at the interface between matrix and reinforcement. Figure 6(c) represents the microstructure of M-3-5 sample. The subfigure (c1) represents the expanded view of Fig. 6(c). BG reinforcement is camouflaged in the Mg-Zn matrix. In contrast, the subfigure (c2) depicts the discontinuities around the matrix reinforcement interface. In Fig. 6(d) and (e), the micropores and BG agglomerated areas are marked in black and white arrows, respectively. The area fraction of micropores and BG agglomerated areas increased relatively with an increase in BG content from 10 to 15%. The void defects were more clearly observable in FESEM micrographs than OM images (refer to Fig. 4). The microstructure obtained in the present study is in accordance

with recent findings. The mechanical properties of Mg and Mg-BG composites without zinc addition using spark plasma and hot pressing techniques was evaluated (Ref 10, 11). In contrast, the present study highlights the role of zinc in enhancing the mechanical properties of Mg-Zn-BG composites.

3.5 EDS and XRD Analysis of Sintered Composites

All the compositions of the Mg composites were examined using energy dispersive spectroscopy (EDS) and represented in Fig. 7(a)-(e). Oxygen was found to be present in the spectrum data of all the compositions. Indeed, the most significant percentage of Oxygen was found in BG reinforced composites because of the presence of oxides in the BG reinforcements, Fig. 7(c)-(e). The presence of zinc was around 4-6% in Mg-Zn matrix-based composites. A fraction of 1% zinc was observed in M-3-15, attributing it to the lesser metal matrix area being exposed for the analysis. The wt.% of Si in the spectrum was found to increase with an increase in BG content in the composites. The point and shoot approach was used to determine the presence of specific phases and to discern information at a particular area of interest. MgZn matrix phase was noticed at point 2 in M-3-0, point 4 in M-3-5, point 3 in M-3-10 and point 4 in M-3-15. Point 3, point 1 and point 1, 2 in M-3-5, M-3-10 and M-3-15, respectively, were found to be silicon-rich phases. Among them, a possible Mg_2Si phase was observed in point 3 in M-3-5. It is difficult to exactly assert the presence of pure Mg_2Si or MgO phases from the EDS approach but can be predictively stated. The addition of BG to 3 wt.% Zinc decreased the % of Zinc according to EDS. This might be probably due to the fact that BG enhanced the solubility of Zinc in Mg. To confirm the phases present in the sintered composites, XRD was carried out on all sintered composites. The peaks of Mg-BG and Mg-Zn-BG composites are depicted
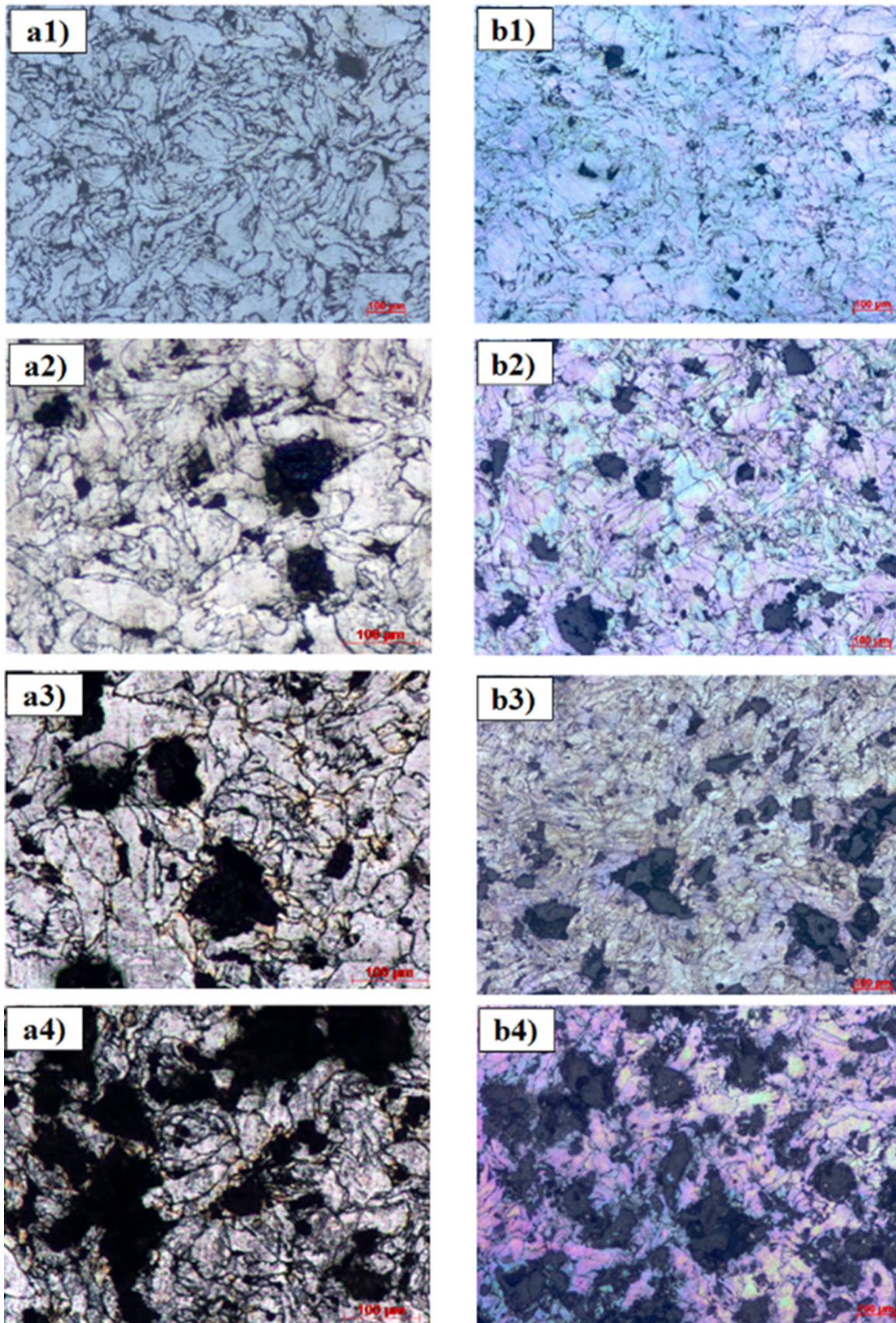
Fig. 4 Optical Microscopic images of sintered composites without 3% Zn-(a1) M-0-0, (a2) M-0-5, (a3) M-0-10, (a4) M-0-15, and with 3% Zn-(b1) M-3-0, (b2) M-3-5, (b3) M-3-10, (b4) M-3-15
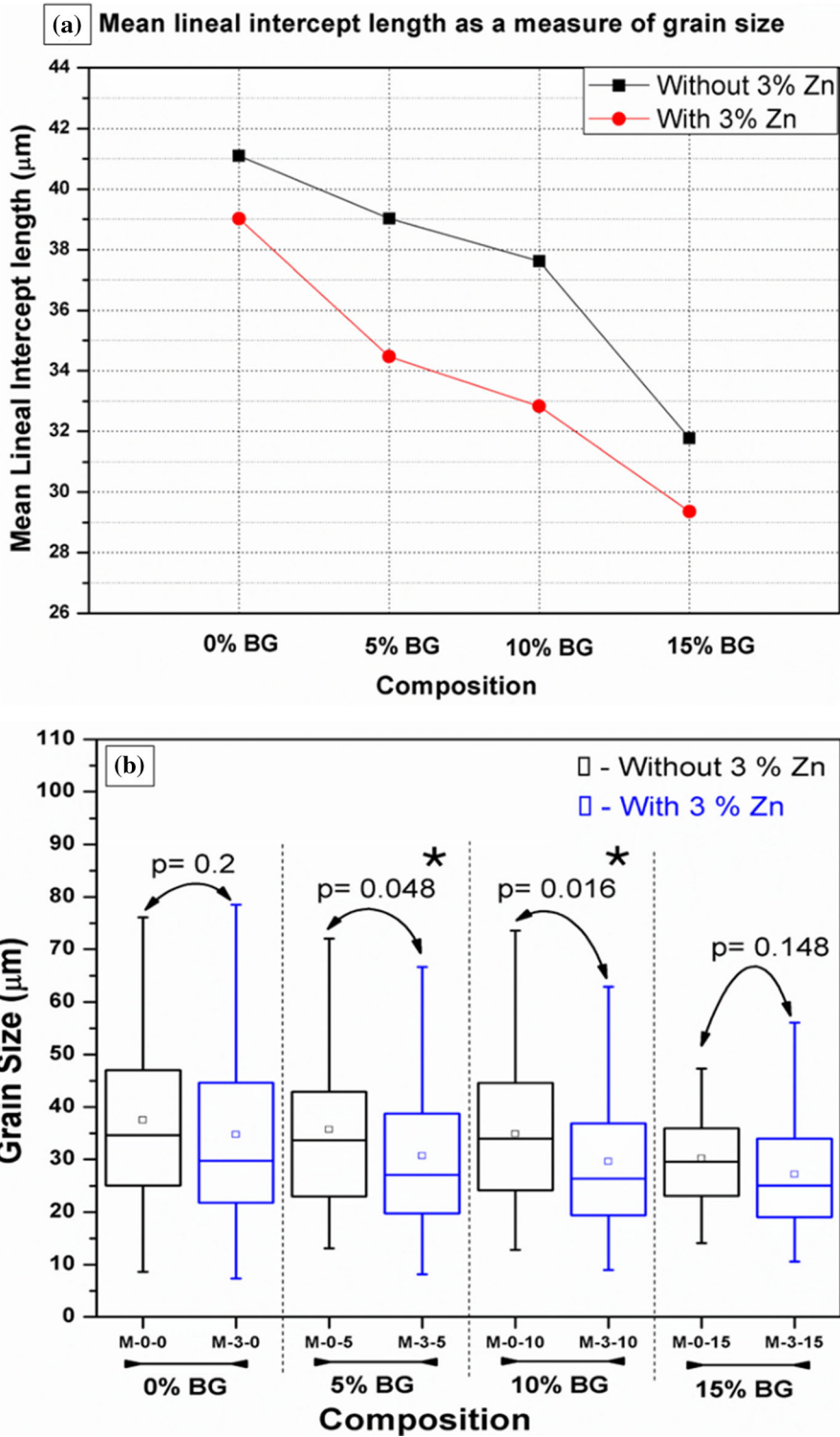
Fig. 5 Grain size analysis plots of the composites (a) Representation of variation of mean linear intercept length as a measure of grain size for different compositions; (b) Grain size distribution represented in box plots for different compositions (*-Statistically significant)

in Fig. 8(a) and (b), respectively. From Fig. 8(a) the following observations are made (i) for M-0-0 sample, there were no specific phases except Pure Mg was detected (ii) in addition to Mg phase, Mg_2Si phase was detected in M-0-5, M-0-10 and M-0-15 samples. From Fig. 8(b) one can observe that (i) in M-3-0 sample peaks corresponding to Mg phase coexisted with MgZn phase (ii) three phases Mg, MgZn and Mg_2Si evinced in M-3-5,

M-3-10 and M-3-15 samples i.e Mg-Zn-BG samples (iii) Mg, MgZn and Mg_2Si coexisted at 2 Theta value of 73 degrees. The phase predicted from EDS Fig. 7 are confirmed using XRD plot represented in Fig. 8. Thus, composition and phase formation in bulk grain and grain boundaries present in the OM, FESEM images Fig. 4 and 6 of sintered composites are completely revealed by EDS and XRD plots depicted in Fig. 7 and 8. The
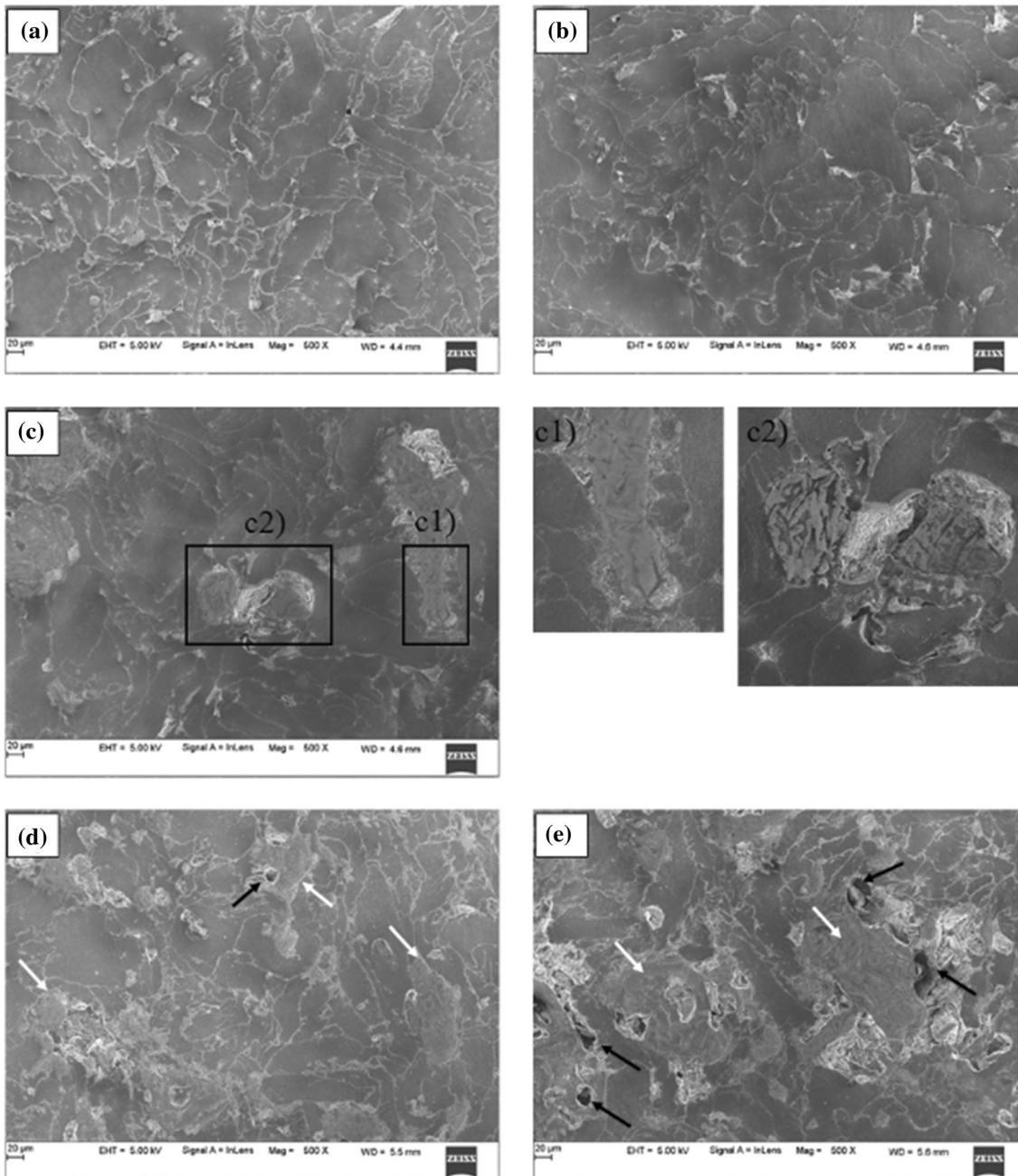
Fig. 6 FESEM micrographs of sintered composites (a) M-0-0, (b) M-3-0, (c) M-3-5, (d) M-3-10 and (e) M-3-15; (Black arrows indicates micro pores, white arrows indicate Bioglass, c1 subfigure shows better bonding between matrix and reinforcement, c2 subfigure shows discontinuities around matrix reinforcement interface-delineation of matrix reinforcement interface)

presence of these phases has a significant effect on the mechanical properties and corrosion behavior of sintered Mg composites.

3.6 Mechanical Characterization of Sintered Composites

3.6.1 Density-Porosity Analysis of Sintered Composites. Analysis of the densification of sintered composites is quite essential to understand its effect on the mechanical properties and corrosion behavior. Theoretical density, measured density and porosity ratio of different compositions are shown in Fig. 9(a)-(b), respectively. From Fig. 9(a), it is clear

that the theoretical density increased chronologically with the addition of BG and combination of Zinc added along with BG. However, the theoretical density of Mg-Zn-BG samples was relatively greater than Mg-BG samples. In contrast, measured densities of all the compositions were less than the theoretical densities of the corresponding compositions. The decrease of measured densities became significant in M-0-10, M-3-10, M-0-15 and M-3-15 samples. Interestingly, the measured density increased from 1.60 in M-0-15 sample to 1.68 for M-3-15 due to the presence of zinc. The relative decrease in measured density is accounted for the voids or pores generated during the

(a)
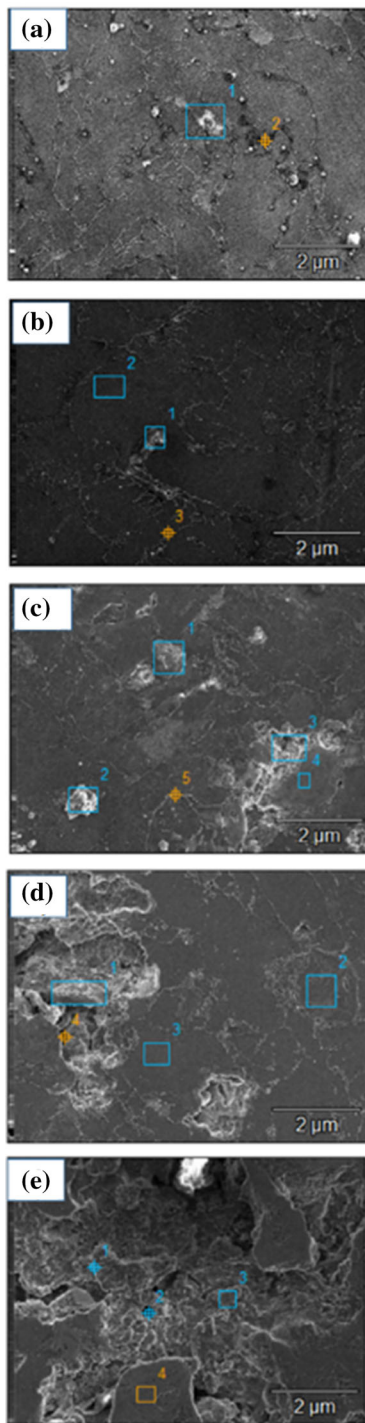
Wt %	O	Mg
Point 1	12.26	87.74
Point 2	5.27	94.73

(b)

Wt %	O	Mg	Zn
Point 1	16.03	78.99	4.98
Point 2	2.55	91.01	6.44
Point 3	18.16	73.84	8.01

(c)

Wt %	O	Mg	Zn	Si	Others – Ca, P, Na
Point 1	22.99	67.8	5.91	02.53	0.78
Point 2	26.89	58.62	6.64	5.73	2.12
Point 3	17.36	67.81		14.83	
Point 4	24.96	67.05	4.46	3.52	
Point 5	8.62	84.06	5.73	0.82	0.76

(d)

Wt %	O	Mg	Zn	Si	Others – Ca, P, Na
Point 1	18.66	59.62	2.18	14.27	5.27
Point 2	23.42	68.01	4.64	2.19	1.75
Point 3	5.34	88.04	5.24	0.38	1.00
Point 4	14.13	71.73	4.64	4.78	4.73

(e)

Wt %	O	Mg	Zn	Si	Others – Ca, P, Na
Point 1	6.73	58.79	0.45	32.74	1.28
Point 2	6.66	60.42	1.09	26.00	5.83
Point 3	11.38	82.84	2.21	2.73	0.84
Point 4	20.34	71.6	2.78	3.44	1.85

Fig. 7 EDS analysis of sintered composites (a) M-0-0 (b) M-3-0 (c) M-3-5 (d) M-3-10 (e) M-3-15

processing of the composites. To get better insights into generated porosities, the porosity ratio of composites are depicted in Fig. 9(b). The porosity ratio of the composites increased chronologically with increase in reinforcements for Mg-BG and Mg-Zn-BG composites. The porosity ratio of M-0-0 sample increased from 3.2 to 4.7% in M-3-0 sample. While the porosity ratio of both M-0-5 and M-3-5 is measured to be ~ 6% which is comparable. In contrast to them, the porosity ratio of M-0-10 sample decreased drastically from ~ 10 to ~ 6% for M-5-10 sample condition. Similarly, the porosity ratio of M-0-15 sample evinced a drop from ~ 11 to ~ 9% in M-3-15 sample. This increase in density of 15% BG samples depicted in Fig. 9(a) is related to the drop in porosity evident from Fig. 9(b). It is well known that the ideal implants should mimic the properties of cortical bone (Ref 17). The cortical or the outer dense layer of bone is reported to exhibit a porosity of ~ 10%. Indeed, this porous nature of bone assists in bone ingrowth, transportation of nutrients and metabolic wastes (Ref
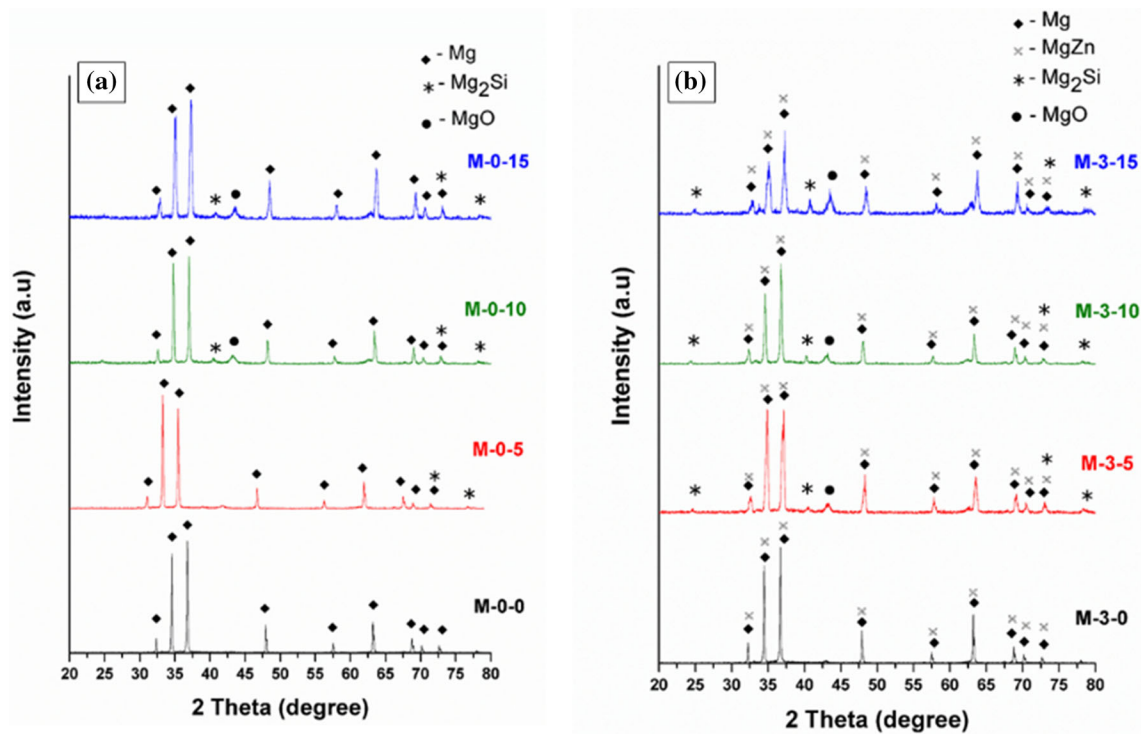
Fig. 8 XRD pattern of sintered metal matrix composites (a) Mg-BG, (b) Mg-Zn-BG

[1, 2, 18]). The composites developed in the present study also a evince porosity ratio of 3.3-8.7% which is comparable to cortical bone. Hence, it is reasonable to believe that the porosity ratio of Mg composites developed in the present study is analogous to human bone.

3.6.2 Influence of Microstructure on Compression Strength of Sintered Composites. The biomaterials used for orthopedic applications are majorly subjected to compressive loads among many other types of loads (Ref 19). Particulate strengthening by adding reinforcements to metallic powders has been considered as one of the major strengthening techniques to improve the mechanical properties. The stress-strain graph of Mg-based sintered composites and mean compressive strength are shown in Fig. 10(a) and (b), respectively. From Fig. 10(a), one can observe that the compressive strength of M-0-0 and M-0-5 samples are 119 and 137 MPa, respectively. The relative increase in compressive strength of 5% BG composites (M-0-5) is corroborated to the presence of Mg_2Si phase depicted in Fig. 8(a). However, M-0-10 and M-0-15 samples evinced a drastic reduction in compressive strength of 103 and 76 MPa when compared to M-0-0 and M-0-5 samples. Surprisingly, these values of compressive strength of M-0-10 and M-0-15 are lower than that of M-0-0 (pure Mg) sample. From, the compressive strength results of Mg-BG samples it is reasonable to believe that Mg_2Si present in BG enhances the compression strength. On the contrary, sintering defects such as micropores and discontinuities around matrix reinforcement deteriorate compression strength. Hence, the results obtained from compression strength tests gives insights into the factor that dominated in each composition. In case of Mg-Zn-BG samples, the compressive strength was found to increase chronologically from 119 MPa for M-0-0 sample to 181, 201 and 205 MPa in M-3-0, M-3-5 and M-3-10.

It should be noted that the compressive strength of M-3-5 and M-3-10 samples are comparable. In contrast, the compressive strength decreased significantly up to $\sim$ 133 MPa for M-3-15 composite. From FESEM micrographs Fig. 6(e) of the sintered composites, it was observed that 15% BG reinforced composites exhibited pores at the interface of matrix and reinforcement. The presence of pores indicates that the porosity ratio was higher for such samples, evident from Fig. 9, density-porosity analysis. The lower compressive strength of 15% BG reinforcements is attributed to a higher porosity ratio, as porosity leads to discontinuity in bonding. In addition to porosity excessive addition of BG resulted in agglomeration. Though porosity for M-3-5, M-3-10 is higher than M-0-0, compressive strength is still higher for BG reinforced composites. This is due to the phenomenon of particulate strengthening and the presence of MgZn, Mg_2Si phases evident from XRD plots represented in Fig. 8(b). With the addition of 3% Zn which is well below the solid solubility limit of Zn in Mg (Ref 12, 13), the MgZn matrix phase is formed, evident from XRD analysis (refer Fig. 8). Due to this microstructural change of phase, there is a significant enhancement in compressive strength. Jaiswal et al. reported that the compressive strength of Mg-3Zn-HA composites were in the range of 116-134 MPa (Ref 7). In addition, it is well known that the compressive strength of human cortical bone is in the range of 100-200 MPa. Duan and co-workers developed a scaffold in which Mg rods were reinforced into BG bone cement composite. They reported a compressive strength of 180 MPa for Mg-BG composites (Ref 17). Knapek et al. obtained compressive yield strength (CYS) 149-189 MPa for WN43 Mg by spark plasma sintering SPS (Ref 20). Dvorský et al. reported CYS of 150 to $\sim$ 200 MPa for WE43 Mg processed by SPS (Ref 21). In the present study, Mg-3Zn-10BG composites, i.e., M-3-10 sample evinced rela-
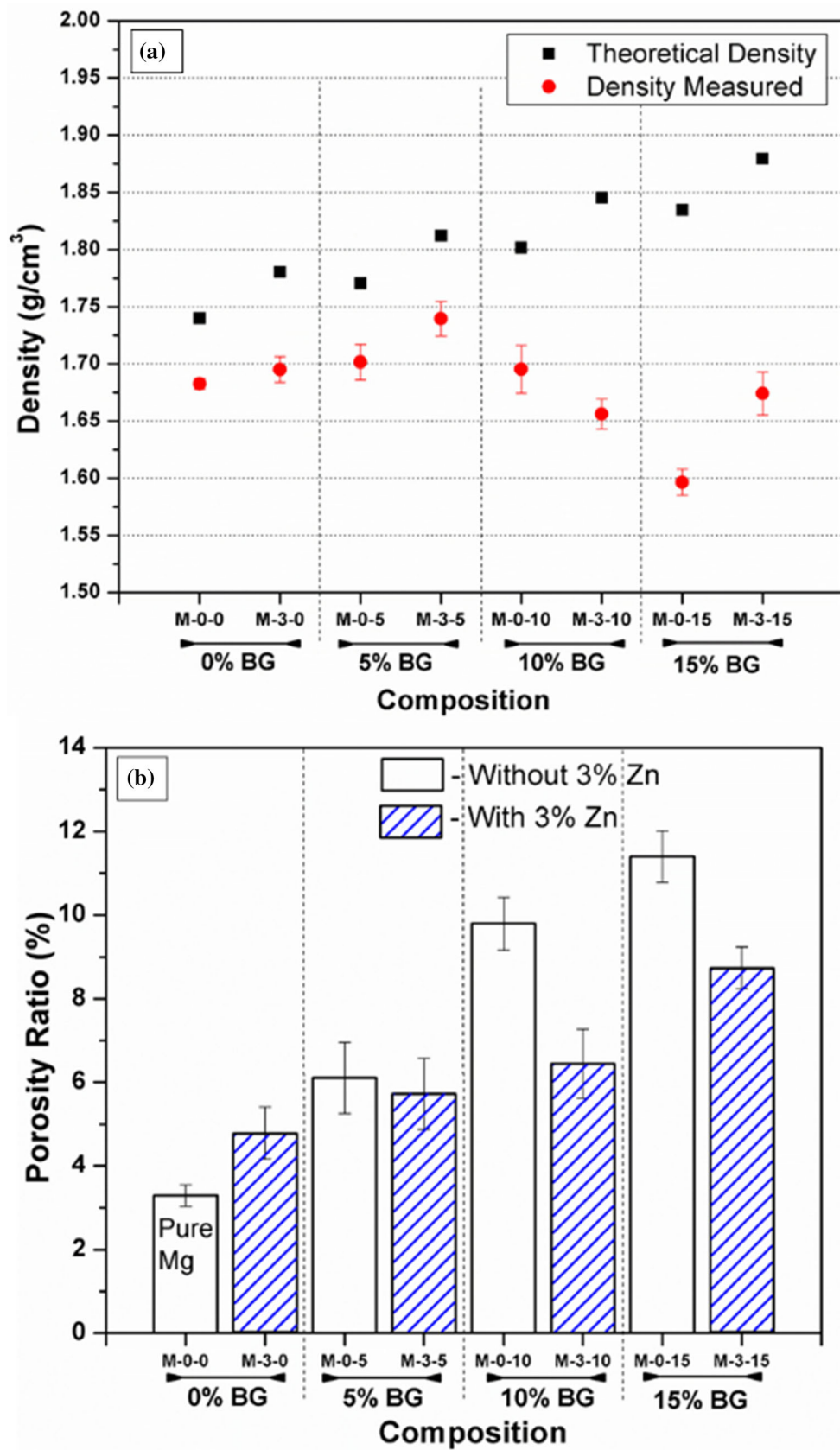
Fig. 9 (a) Theoretical and measured densities of Mg composites; (b) Variation of porosity ratio Mg composites (*-Statistically significant)
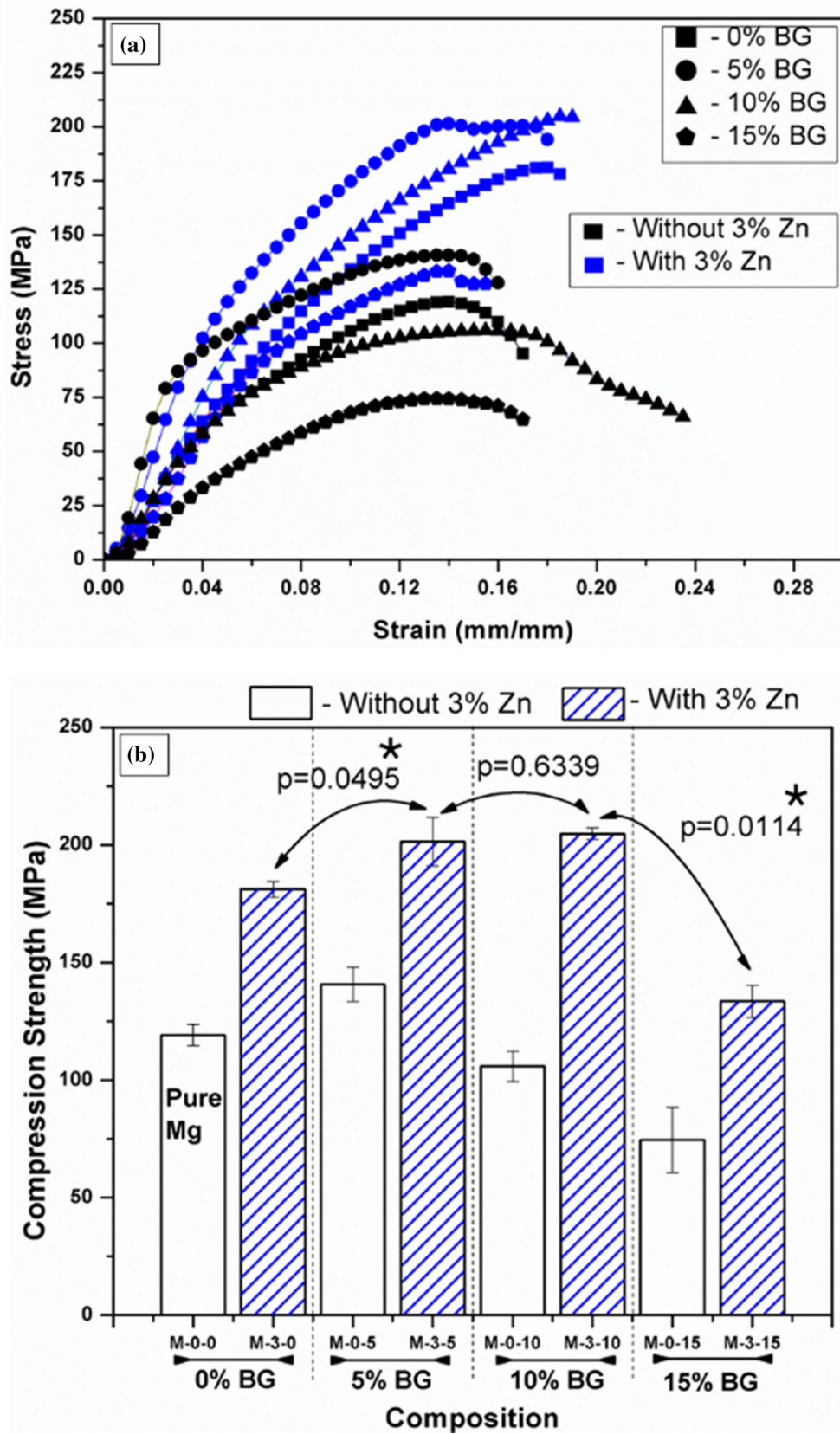
Fig. 10 (a) Stress-Strain graph of Mg composites; (b) Variation of compressive strength of Mg composites (*-Statistically significant)

tively higher compressive strength of 205 MPa. Also, it is well established that the mechanical properties of Mg samples deteriorate in vivo (Ref 14, 22). Hence, the relatively higher compressive strength of M-3-10 samples might assist them in maintaining the mechanical integrity for a relatively longer duration. Thus, based on the present study and open literature (Ref 7, 14, 17, 20-22) it is reasonable to believe that BG enhanced the compressive strength of Mg-based composites to a greater extent than HA.

3.6.3 Effect of Zinc and BG Addition on the Hardness of Sintered Composites.

The hardness values of sintered Mg-BG and Mg-Zn-BG composites are depicted in Fig. 11. The Vickers hardness of M-0-0, M-0-5, M-0-10 and M-0-15 samples are measured to be $\sim$ 59, 71, 76 and 78 Hv. The relative increase in hardness values is associated with Mg_2Si phase present in the Mg-BG composites. It can also be observed that the standard deviation of Mg-BG samples increased with an increase in BG addition due to the variation in porosity ratio (refer to Fig. 9(b)). In the case of Mg-Zn-BG samples, the hardness values of M-0-0, M-3-0, M-3-5, M-3-10, M-3-15 samples were found to be 59, 85.5, 95.3, 97.3 and 99.3 Hv. The hardness values increased significantly with the addition of 3% Zn. The addition of BG further increased the hardness values. However, the hardness values obtained after the addition of 5, 10 and 15% BG were comparable. The addition of BG in an Mg-3Zn metal matrix has a significant effect on improving the hardness values over pure magnesium. This is related to the formation of harder MgZn phase which is evident from Fig. 8, XRD plots of sintered composites. The

further increase in hardness is attributed to the presence of both MgZn and Mg_2Si phases in composites containing BG. In summary, the hardness values of Mg-Zn-BG are significantly higher than that of Mg-BG composites evident from statistical analysis represented in Fig. 11. This is attributed to the presence of MgZn phase and relatively lower porosity exhibited by Mg-Zn-BG composites. Dutta et al. investigated the mechanical properties of Mg after 5, 10 and 15% BG addition. They reported the highest hardness value of 60 HV for Mg with 10% BG addition (Ref 10, 11). It is also noteworthy to mention that, in the present study, M-3-15 sample exhibited the highest hardness value of 99.3 Hv. The hardness values achieved in the present study is relatively higher when compared to the previous studies (Ref 10, 11). This also indicates that zinc along with the combination of BG improved the hardness of Mg composites significantly.

3.7 Electrochemical Corrosion Behavior of Sintered Composites

3.7.1 Properties of Surface Film Developed in Mg-BG and Mg-Zn-BG Composites.

Figure 12(a) and (b) depicts the Nyquist plot of sintered Mg-BG and Mg-Zn-BG composites, respectively. Nyquist plot of Mg-BG and Mg-Zn-BG composites exhibits two capacitive loops: one at high frequency and the other at a medium-frequency and a low-frequency inductive loop. It is well known that the high frequency capacitive loop is related to the charge transfer resistance (R_{ct}). While medium frequency capacitive loop is attributed to the transportation of ions between the metal surface and the
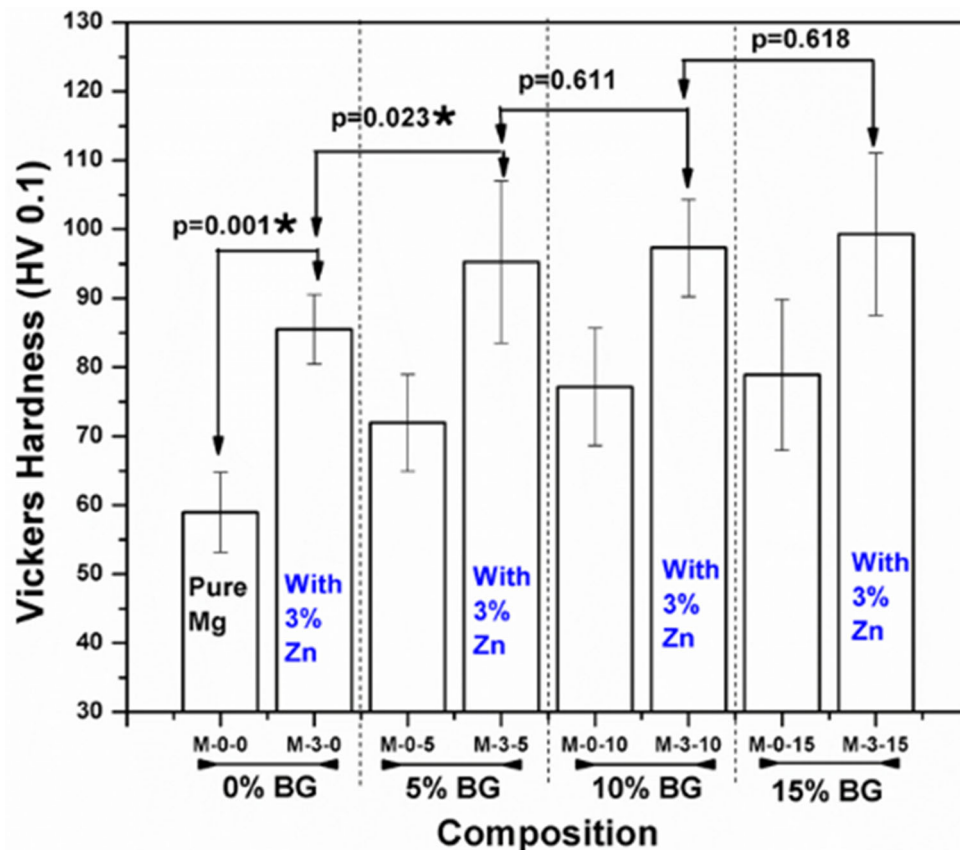

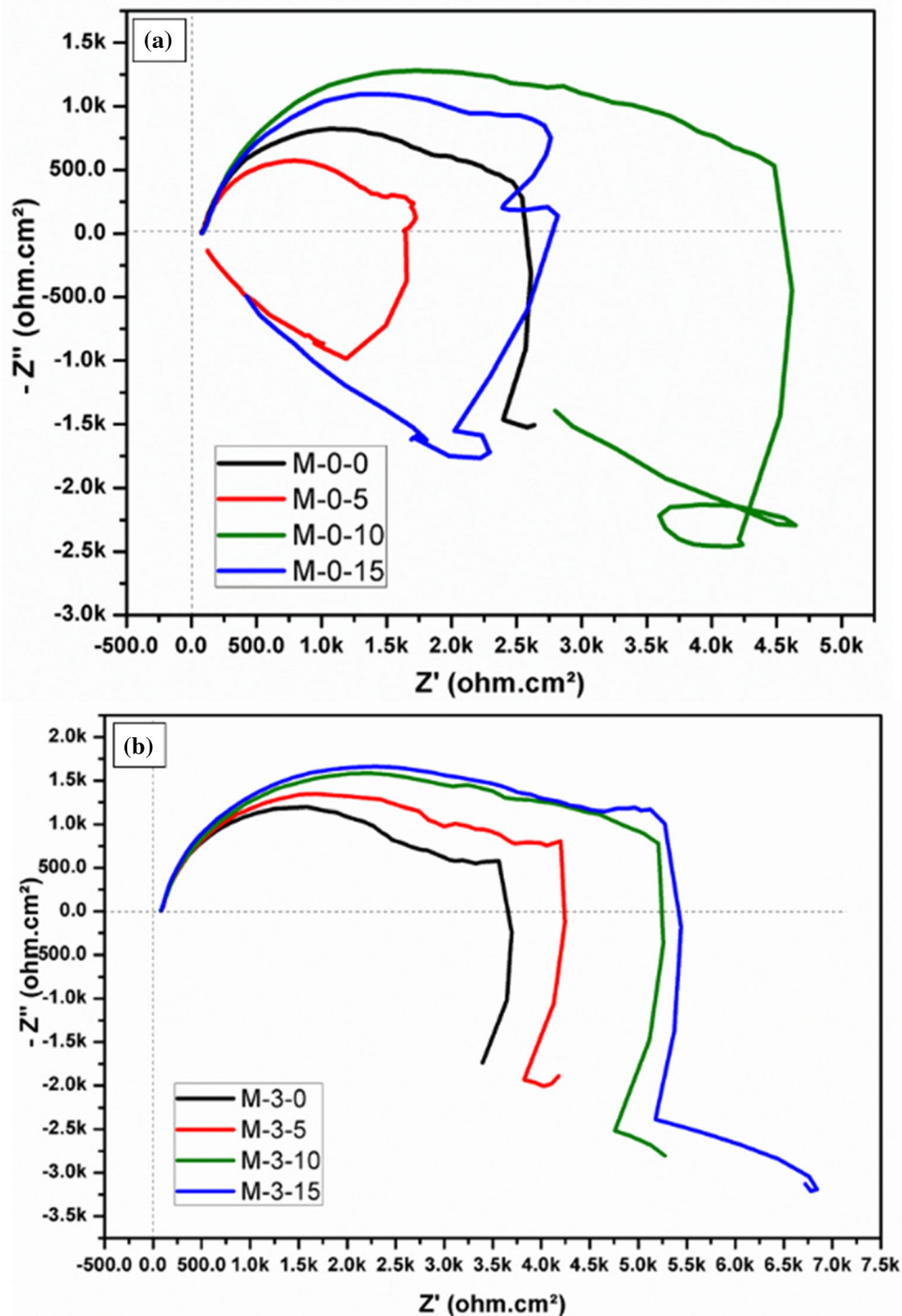Fig. 11 Vickers hardness plots of Mg composites (*-Statistically significant)

Fig. 12 Nyquist plots of different Mg composites (a) Mg-BG (b) Mg-Zn-BG

corrosive medium involved, respectively. While the low frequency inductive loop is generally related to the adsorption process (Ref 23-25). An equivalent electrical circuit was employed in this study to analyze the influence of corrosion parameters such as charge transfer resistance (R_{ct}), solution resistance (R_{sol}) and double-layer capacitance (C_{dl}) and the values are plotted in Fig. 13(a)-(c), respectively. In general, the diameter of the capacitive loops is associated with the corrosion resistance of the material. The larger the diameter of the

capacitive loop, better is the corrosion resistance of the material. From Fig. 12(a), it is evident that the diameter of capacitive loops is ranked as follows M-0-5 < M-0-0 < M-0-15 < M-0-10. The values of charge transfer resistance also followed the same trend as evident from Fig. 13(a). From Fig. 13(b), the solution resistance (R_{sol}) of Mg-BG samples were observed to be in the range of 72-82 ohm.cm^2. The values of double-layer capacitance (C_{dl}) varied in the range of 30-40 μF. The M-0-5 sample evinced relatively lower corrosion
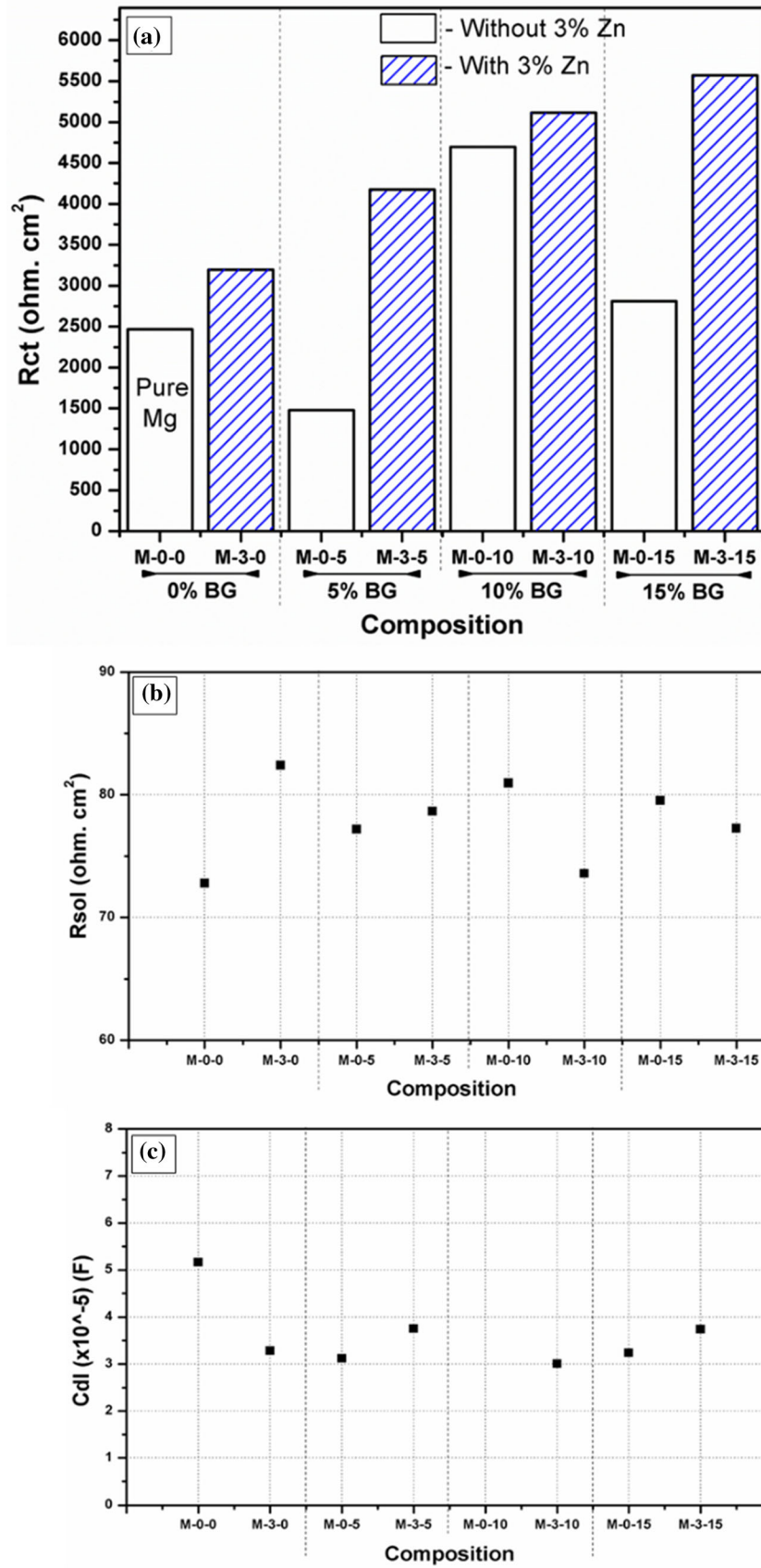
Fig. 13 (a) Charge transfer resistance, (b) Solution resistance, (c) Double-layer capacitance values of Mg composites
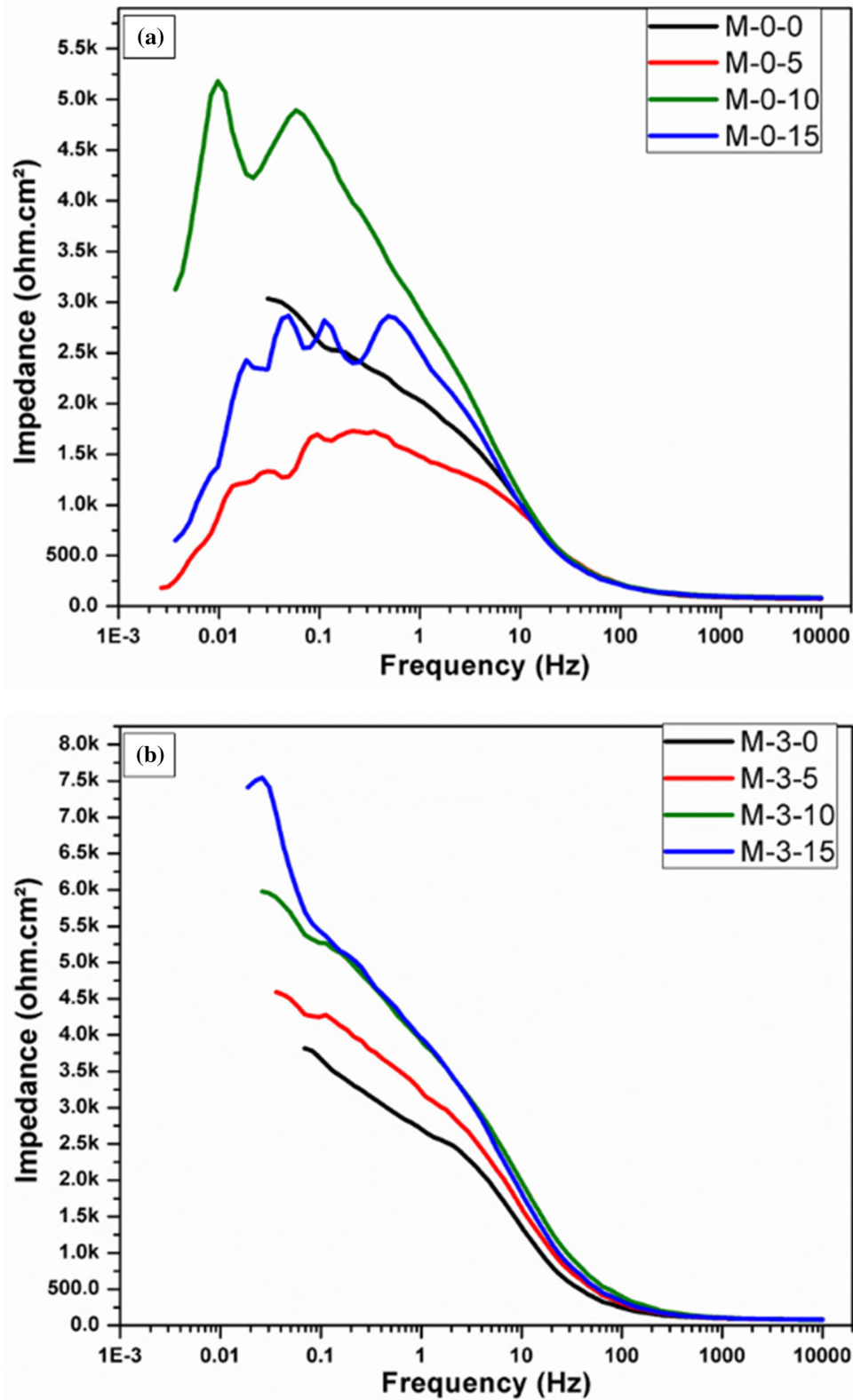
Fig. 14 Bode plots of different Mg composites (a) Mg-BG (b) Mg-Zn-BG

resistance than that of M-0-0 samples. It is related to the relatively higher porosity of M-0-5 samples compared to M-0-0 samples. Another possible reason is that 5% addition of BG in Mg (M-0-5) is not sufficient to increase the corrosion resistance in Mg-BG samples. In contrast, the corrosion resistance of M-0-10, M-0-15 samples are relatively better than that of M-0-0 sample. Hence, it is reasonable to believe that 10% and 15% BG addition in Mg matrix is sufficient to increase corrosion

resistance of M-0-0 sample even though their porosity ratio is higher than M-0-0 samples (refer Fig. 9(b)). In contrast for Mg-Zn-BG samples, the diameter of the capacitive loop increased chronologically with increase in BG addition. The Nyquist plot of Mg-Zn-BG samples are presented in Fig. 12(b). From Fig. 13(a), R_{ct} values of M-0-0, M-3-0, M-3-5, M-3-10, M-3-15 samples were calculated to be 2468, 3199, 4178, 5116 and 5572 ohm.cm^2, respectively. From, the Nyquist plots depicted in Fig. 12(b), it also observed that the diameter of the capacitive loops increase chronologically from M-3-0 to M-3-15. This indicates that the corrosion resistance of the sintered Mg composites follows the chronological order, i.e., M-0-0 < M-3-0 < M-3-5 < M-3-10 < M-3-15. The double-layer capacitance (C_{dl}) is indirectly proportional to thickness of double-layer film. Hence, a lower value of C_{dl} also assists in enhancing corrosion resistance. The double-layer capacitance (C_{dl}) values were found to be 51, 32, 37, 30, 37 μF for M-0-0, M-3-0, M-3-5, M-3-10, M-3-15 samples, respectively. The R_{sol} values range from 72 to 82 ohm.cm^2 for sintered Mg composites, i.e., there is no significant changes in the values. This is also clearly visible from the origin point of Nyquist plots. Hence, R_{sol} did not impact the corrosion process to a greater extent. However, it is well established that the impedance is a function of charge transfer resistance (R_{ct}), solution resistance (R_{sol}) and double-layer capacitance (C_{dl}).

3.7.2 Effect of Zinc and BG Addition on the Impedance of Mg-Based Composites.

Bode impedance plots of Mg-BG and Mg-Zn-BG composites are depicted in Fig. 14(a) and (b), respectively. They are generally divided into high-frequency (10,000-100 Hz), medium-frequency (100-1 Hz) and low-frequency regions (1-0.001 Hz). From Fig. 14(a), it can be observed that at high frequency region Mg-BG samples did not show any significant difference in behavior up to 10 Hz. The M-0-0 sample evinced a linear increase in impedance from 1500 ohm.cm^2 at 10 Hz to ~ 3000 ohm.cm^2 at 0.01 Hz. On the contrary, M-0-5, M-0-10 and M-0-15 samples exhibited a linear increase in impedance values to 0.1 Hz and then dropped down to significantly lower values of impedance by the end of 0.01 Hz. This drastic reduction in impedance values observed in Mg-BG composites signifies pitting formation. This in turn is related to the porosity of Mg-BG composites (refer to Fig. 9). However, the impedance values were measured to be 3000, 245, 3220 and 720 ohm.cm^2 for M-0-0, M-0-5, M-0-10 and M-0-15, respectively. The trend of impedance values obtained from Bode plots are in line with Nyquist plots (Fig. 12(a)). The Bode impedance plots of Mg-Zn-BG composites are depicted in Fig. 14(b). The impedance values of Mg-Zn-BG composites increased steadily with increase in frequency. However, the variation in values of impedance became significant in the frequency range of 10-0.01 Hz. The impedance values 3814, 4595, 5982 and 7425 ohm.cm^2 corresponds to M-3-0, M-3-5, M-3-10, M-3-15 Mg sintered composites, respectively. Similar trends in impedance values were observed when ZM21 Mg was subjected to EIS after different immersion timings in Ringer's solution (Ref 26).

Potentiodynamic polarization (PDP) curves of sintered Mg-BG and Mg-Zn-BG composites are shown in Fig. 15(a) and (b), respectively. From Fig. 15(a), it is apparent that Mg and Mg-BG samples exhibited a slight deviation in Tafel behavior due to anodic hydrogen evolution. It is also observed that with addition of BG the potential shifted to noble values. However, the corrosion current densities of Mg-BG samples were relatively higher than that of pure Mg sample. The corrosion rates of Mg

and Mg-BG samples measured based on the cathodic slope of Tafel plot are depicted in Fig. 16. The corrosion rate of M-0-0, M-0-5, M-0-10 and M-0-15 samples are calculated to be 1.2, 4.3, 1.4 and 3.4 mm/year, respectively. The trend of corrosion obtained from Tafel plots are in reasonable agreement with impedance plots, Fig. 14(a). The Tafel plots of Mg-Zn-BG composites are represented in Fig. 15(b). M-3-0, M-3-5, M-3-10, M-3-15 samples deviated from ideal Tafel behavior due to the well-established anodic hydrogen evolution phenomenon in Mg alloys. It is also clearly visible that due to zinc and BG addition the potential values shifted in the positive direction. However, the corrosion rate generated from potentiodynamic curves gives better insights quantitatively. Corrosion rate interpolated from potentiodynamic plots (PDP) are shown in Fig. 16. The corrosion rate of M-0-0 sample calculated from PDP plots was 0.71 mm/yr. The corrosion rates of M-3-5, M-3-10, M-3-15 were calculated to be 1, 0.39 and 0.41 mm/yr, respectively. The corrosion resistance based on PDP curves is ranked in the following order M-3-10 ~ M-3-15 ~ M-3-0 > M-0-0 > M-3-5. In contrast, the EIS plots exhibited a chronological increase in corrosion resistance, i.e., M-3-15 > M-3-10 > M-3-5 > M-3-0 > M-0-0. In summary, Mg-Zn-BG samples exhibited better corrosion resistance than Mg-BG samples. However, M-3-10 sample exhibited the highest corrosion resistance among all. This is attributed to the relatively lower porosity (Fig. 9) and sufficient BG content that acted as a partial coating on the surface of Mg-Zn-BG composites. The corroded surface morphology of Mg-Zn-BG samples are depicted in Fig. 17. The surface of M-0-0 sample evinced random discontinuities observed in Fig. 17(a) probably due to the penetration of PBS medium into the sample. M-3-0 sample also exhibited discontinuities which were concentrated in particular area as evident from Fig. 17(b). This is corroborated to the undermining of MgZn secondary phases due to activation of micro-galvanic corrosion between Mg and MgZn phase. In contrast, the corroded surface of M-3-5, M-3-10 and M-3-15 samples remained unaffected from effect of destructive nature of chloride ions and micro-galvanic corrosion occurring between Mg and MgZn phase. This is related to the presence of Mg$_2$Si phase in M-3-5, M-3-10 and M-3-15 samples. Mg$_2$Si acts like a partial coating and dominates the activity of chloride ions and micro-galvanic corrosion. The slight variation in trends obtained from EIS and PDP plots is attributed to variation in method of corrosion resistance evaluation. EIS considers the properties of surface film, i.e., impedance and is non-destructive. In contrast, the PDP considers the anodic, cathodic behavior, i.e., electrochemical and chemical corrosion of Mg. Also, in electrochemical corrosion studies, the sample exposure area and time are limited to a maximum of 5 h. Hence, in the present study immersion tests up to 3 days were carried out to get better insights into corrosion of sintered composites. The corrosion rate obtained in the present study is relatively higher than Mg-BG composites processed by Dutta et al. (Ref 11, 12). This is corroborated to the presence of MgZn phases which increases the dissolution rate of Mg composites due to the formation of micro-galvanic cells.

3.8 Immersion Corrosion Behavior of Sintered Mg Composites

Corrosion rate of different compositions at different immersion time is represented in Fig. 18. Magnesium corrosion is dynamic in nature because two important processes occurs simultaneously. The chloride ions present in PBS causes
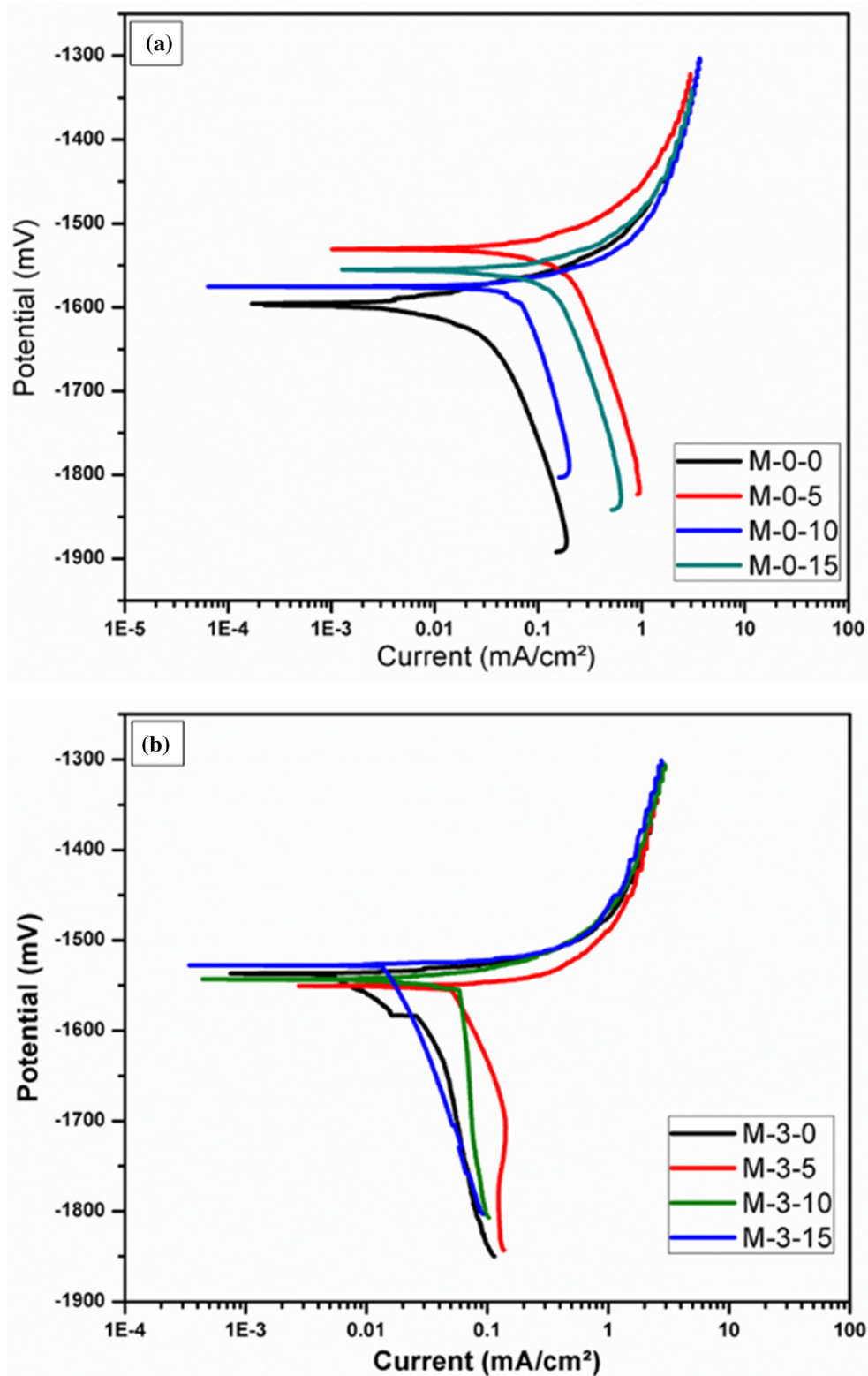
Fig. 15 Tafel plots of different Mg composites (a) Mg-BG (b) Mg-Zn-BG

dissolution of Mg. While, a partially protective $Mg(OH)_2$ layer developed on the surface of Mg inhibits corrosion (Ref 27, 28). The corrosion rate of M-0-0 was found to increase with the increase in immersion time from 10.95 mm/yr in 24 h to 27.38 mm/yr after 72 h of immersion in PBS. The increase was sharp at 72 h immersion which is corroborated to the destruc-tive nature of chloride ions present in PBS, porosity ratio of 3.3% and the absence of BG. With the addition of 3% zinc and BG, the corrosion process becomes complicated. This is due to the following reactions occurring at Mg and PBS interface (i) chloride ions destroy the Mg surface (ii) corrosion inhibition is provided by $Mg(OH)_2$ film and BG which acts as a partial
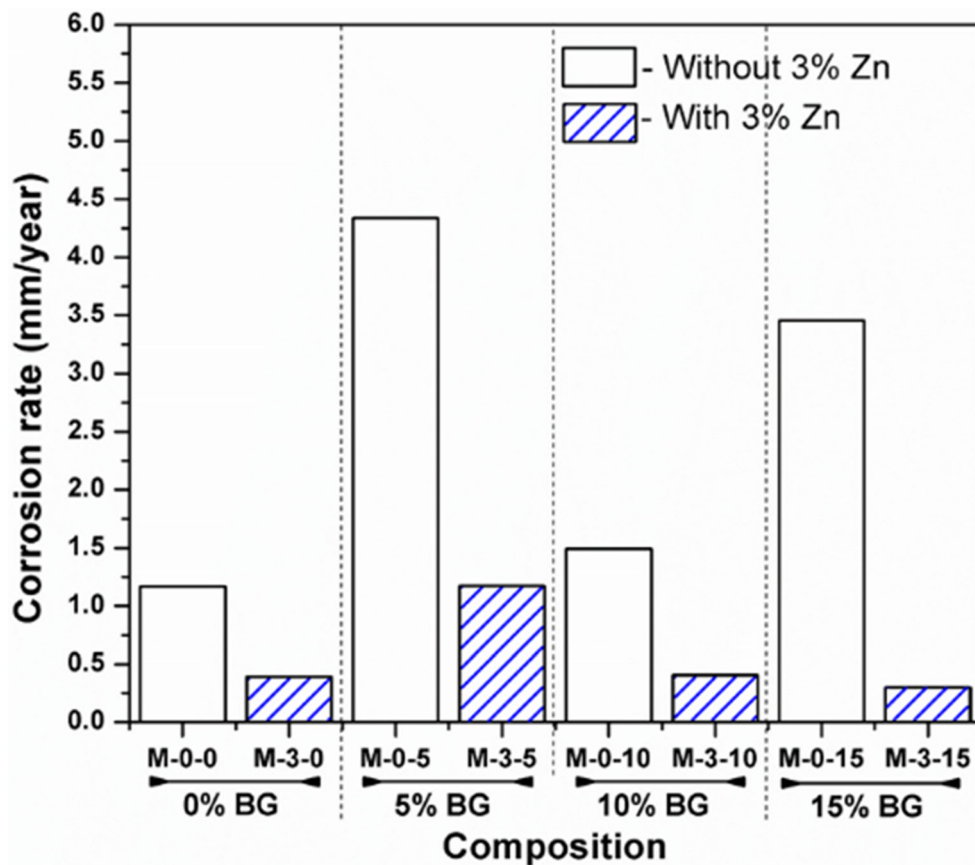
Fig. 16 Corrosion rate of Mg composites measured based on Tafel extrapolation technique

coating. The corrosion rate of the composites M-3-5, M-3-10 and M-3-15 decreased significantly for all three immersion times of 24, 48 and 72 h. This is due to the fact that effect of corrosion inhibition exhibited by combination of $Mg(OH)_2$ and BG was more pronounced than destructive nature of chloride ions. Even though, M-0-0 sample exhibited the lowest porosity ratio the corrosion rate was found to be the highest among all samples. In contrast, porosity ratio of M-3-0, M-3-5, M-3-10 and M-3-15 increased with increase in BG addition. This indicates that in general the effect of porosity was minimal on corrosion resistance. However, after 72 h of immersion, the corrosion rate of M-3-15 is relatively higher than M-3-10. This signifies that after 72 h of immersion the influence of porosity became predominant. In general, the addition of BG decreased the corrosion rate of the composites with M-3-10 composition showing the least corrosion rate of 2.53 mm/yr at 72 h of immersion. The pH of the corrosion medium was found to increase from a pH of 7.4 before sample immersion to a pH of 11-12. The higher value of pH is attributed to chemical reactions that occur during the degradation of Mg. Mg reacts with the aqueous solution to form magnesium hydroxide $(Mg(OH)_2)$ and release hydrogen (H_2) gas. Thus, the pH of the corrosion environment increases for Mg-based materials. The pH of the corrosion medium was showing an increasing trend with increase in time periods for all the compositions except M-3-10. pH of the corrosion medium showed a decreasing trend after 48 h immersion, indicating a decrease in degradation tendency which was also evident from corrosion rate. Also, it is well established that the $Mg(OH)_2$ attains stable state pH above

11. The corrosion rate of Mg sintered samples calculated from PDP curves are in the range of 0.3-1 mm/year. In contrast, the corrosion rate was found to be in the range of 2.50-27.38 mm/yr for immersion tests. This significantly large difference in corrosion rate obtained from PDP and immersion tests is due to the variation in sample surface area, sample immersion time periods as well as the technique in which corrosion rate is calculated. SEM micrographs of the corroded samples for all the compositions, after 24, 48 and 72 h of immersion is depicted in Fig. 19. The morphology of M-0-0 sample appears to be severely corroded at 24, 48 and 72 h duration evident from Fig. 19(a)-(c), respectively. From, the corrosion rate of M-0-0 sample calculated based on immersion tests it is reasonable to believe that entire surface is undermined. It can be observed from Fig. 19(d)-(f) that M-3-0 exhibited corrosion only along grain boundaries but bulk Mg region remains was not attacked. The fine distribution of MgZn phase in Mg inhibited the corrosion even after a prolonged duration of 48 and 72 h of immersion. Also, the pH value was in the range of 11 which maintained the robustness of $Mg(OH)_2$ film. In case of M-3-5 samples, majority area of sample was not corroded at all up to 24 h. The corrosion progressed over the entire surface uniformly by the end of 48 and 72 h as seen from Fig. 19(g)-(i). Further addition of BG, i.e., in M-3-10 samples filiform corrosion was observed almost along the entire surface at 24 h. However, after 48 and 72 h duration, the mode of corrosion was uniform in nature which is evident from Fig. 19(j)-(l). It can be observed from the corrosion morphology that the M-0-0 and M-3-15 samples are exhibiting higher morphological
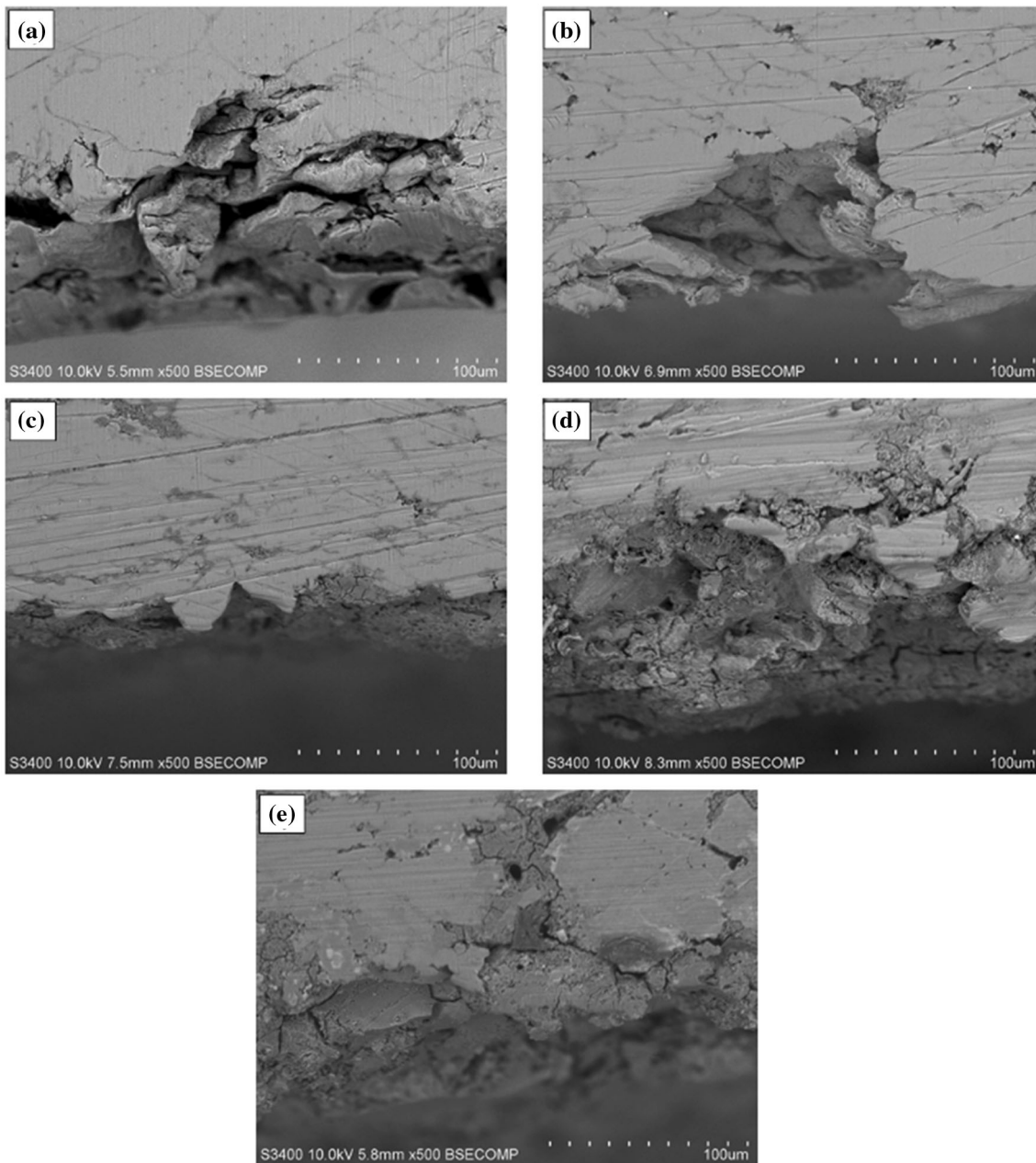
Fig. 17 SEM micrographs of corroded Mg composites tested for electrochemical corrosion study in PBS medium (a) M-0-0, (b) M-3-0, (c) M-3-5, (d) M-3-10, (e) M-3-15

changes compared to M-3-0, M-3-5 and M-3-10. This might be corroborated to the fact that BG acts like a coating on surface of Mg composites. However, in M-3-15 the corrosion was severe when compared to M-3-0, M-3-5 and M-3-10 samples. This is related to the relatively higher porosity ratio of M-3-15 samples. The Mg ions present in PBS solution after 24, 48 and 72 h immersion of Mg-Zn-BG composites obtained using atomic absorption spectroscopy (AAS) are tabulated in Table 2. The Mg ion release decreased significantly from 24 to 48 h immersion. While, Mg ion release increased relatively by the end of 72 h immersion. Indeed, the rank of Mg ion release is as follows 24 > 72 > 48 h. However, the trend of corrosion

rates evaluated from weight loss method is not in good agreement with Mg ion release obtained from AAS for 24, 48 and 72 h immersion. This variation in trend of corrosion rate might be attributed to the differences in their evaluation technique in addition to dynamic nature of Mg corrosion. In summary, the corrosion rates obtained from immersion tests are in good accordance with the corrosion morphology of Mg composites. Lim PN et al. produced Mg-1Ca/HA composites with 5, 10 and 15% of HA using a blending technique. Among the composites investigated, Mg-1Ca-10 HA exhibited better biomechanical properties (Ref 29). Kumar et al. (2020) developed Mg15Nb3Zn1Ca composite by vibrations generated
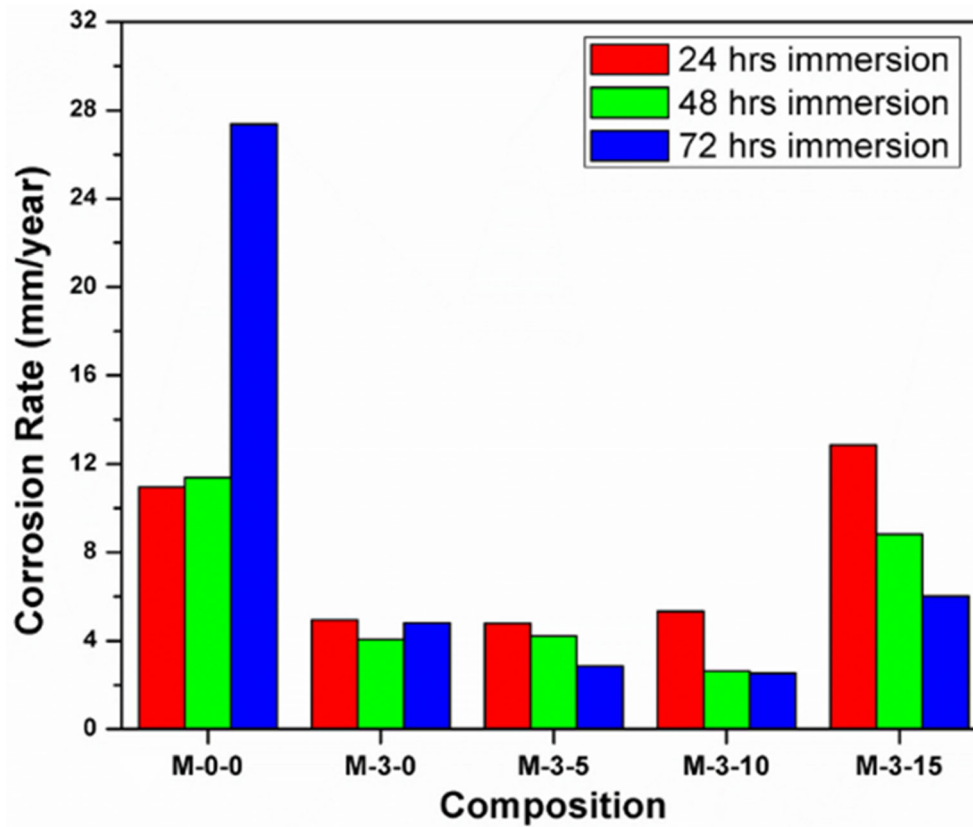
Fig. 18 Corrosion rate of Mg composites at varying immersion duration with PBS as corrosion medium
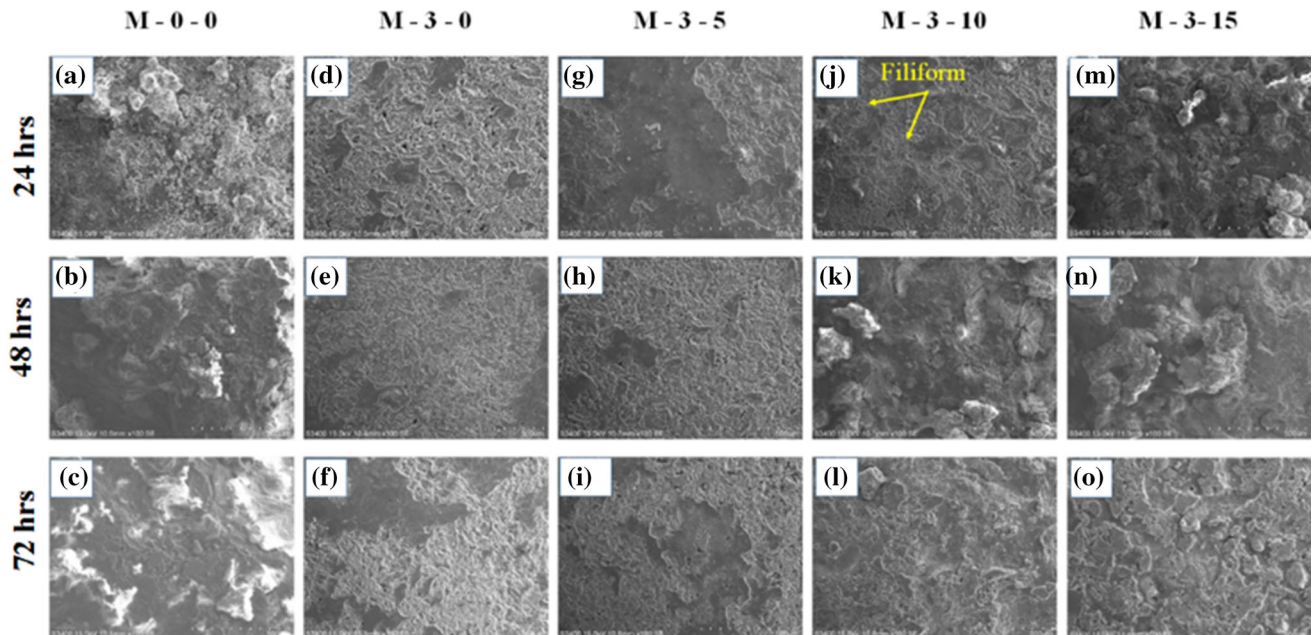

Fig. 19 Corrosion morphology of Mg and Mg-Zn-BG composites

from ultrasonic-assisted sintering technique. However, the weight loss of Mg15Nb3Zn1Ca composites increased with an increase immersion from 2 to 12 h due to formation of micro-galvanic cells (Ref 30). Kang M et al. investigated the biomechanical properties of porous Mg produced by combina-tion of space holder method and spark plasma sintering followed by HA coating. They concluded that HA coating improved the corrosion resistance of Mg samples despite the different levels of porosity ratio of 50, 60and 70% (Ref 31).

3.9 Mechanism of Corrosion in Mg and Mg-Zn-BG Composites

Figure 20 represents the schematic illustration of corrosion mechanism occurring in Mg and Mg-Zn-BG composites in interaction with PBS. It is well established that magnesium corrodes by electrochemical and chemical reactions. Also, a partially protective $Mg(OH)_2$ surface film is generally formed in interaction with electrolyte. This phenomenon represented in the form of Eq 1 to 5. PBS contains 9 g/l of sodium chloride and it interacts with Mg. The chloride ions present in PBS are aggressive in nature. They destroy the partially protective $Mg(OH)_2$ surface film. In case of pure Mg, i.e., M-0-0 sample

Table 2 Mg content (ppm) present in Mg-Zn-BG composites after various immersion duration

Sample Code	Magnesium content, ppm		
	24 h	48 h	72 h
M-0-0	132.54	72.51	86.91
M-3-0	81.195	59.145	318.57
M-3-5	218.73	56.58	149.76
M-3-10	280.833	60.285	149.76
M-3-15	203.16	75.465	91.125

there is no secondary phases as observed from microstructure, EDS and XRD analysis. The chloride ions continuously destroy the $Mg(OH)_2$ surface film very easily. The corrosion rate of M-0-0 sample after 24, 48 and 72 h of immersion is relatively higher in comparison with other samples. The corrosion morphology represented in Fig. 19 is also in accordance with corrosion rate depicted in Fig. 18. In contrast, from the microstructure, EDS and XRD analysis of Mg-Zn-BG sintered composites MgZn, MgO and Mg_2Si are found.

$$2H^+ + 2e = H_2 (\text{cathodic partial reaction}) \tag{Eq 1}$$

$$2Mg = 2Mg^+ + e \ (\text{anodic partial reaction}) \tag{Eq 2}$$

$$2\,Mg^+ + 2\,H_2O = 2Mg^{2+} + 2OH^- + H_2 (\text{chemical reaction}) \tag{Eq 3}$$

$$2\,Mg + 2H^+ + 2\,H_2O = 2Mg^{2+} + 2OH^- + 2H_2 (\text{overall reaction}) \tag{Eq 4}$$

$$Mg^{2+} + 2OH^- = Mg(OH)_2 (\text{product formation}) \tag{Eq 5}$$
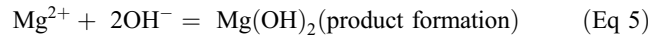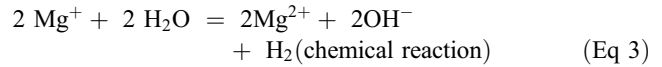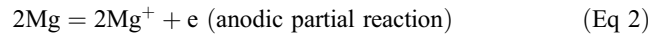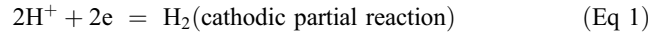
Mg_2Si is formed as result of interaction of BG with PBS. Thus, in case of Mg-Zn-BG sintered samples a composite layer containing partially protective $Mg(OH)_2$ and BG inhibits the
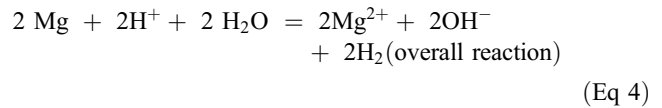

Fig. 20 Corrosion mechanism of Mg and Mg-Zn-BG composites

corrosion process. Hence, in general the corrosion rate of Mg-Zn-BG composites are found to be lower than the pure Mg samples. However, M-3-15 samples exhibited a relatively higher corrosion rate than M-3-5 and M-3-10 samples due to the relatively higher porosity ratio. Hence, it is reasonable to believe that the BG addition formed a partial coating and hindered the corrosion process (Ref 32). However, the influence of porosity becomes predominant in 15% BG addition, i.e., in M-3-15 samples. Thus, the corrosion process in Mg and Mg-Zn-BG sintered samples is influenced by the combination of secondary phases, porosity ratio, chloride ions concentration and robustness of $Mg(OH)_2$ and BG content.

4. Conclusion

The objective of the current work is to enhance the mechanical properties and corrosion behavior of magnesium-based materials for use in biomedical applications, specifically for orthopedic fracture fixative application. In view of the above, the powder metallurgy route was employed by developing a metal matrix composite through the vacuum sintering technique. Zn was added in 3% to Mg-BG metal matrix composite with varying weight fractions of bio glass (BG). The mechanical properties of Mg-BG and Mg-Zn-BG composites were investigated individually and compared.

1. Magnesium (Mg), Bio glass (BG) and Zinc (Zn) powders exhibited mean particle sizes of 183.72, 62.59 and 5.74 μm, respectively. A relatively better compaction was achieved in Mg-Zn-BG composites because the smaller BG and Zn reinforcements accommodated the interstices of Mg matrix.
2. The compressive strength of Mg-Zn-BG samples were significantly higher than Mg-BG samples. Interestingly, M-3-10 sample exhibited the highest compressive strength of 205 MPa among all Mg-BG and Mg-Zn-BG samples. This is related to the combination of solid solution strengthening and particulate strengthening offered by MgZn and Mg_2Si phases, respectively.
3. The Vickers hardness of Mg-Zn-BG samples were also significantly higher than the corresponding Mg-BG samples. The Vickers hardness values of M-3-5, M-3-10 and M-3-15 samples were measured to be $\sim$ 100 Hv. This is attributed to better grain refinement and the presence of Mg_2Si phase in Mg-Zn-BG samples.
4. M-3-10 sample exhibited the lowest corrosion rate of 0.39 mm/yr in electrochemical corrosion tests. The corrosion rate obtained for M-3-10 sample from immersion tests were 4.1, 2.2 and 1.9 mm/year for 24, 48 and 72 h of immersion, respectively. In summary, M-3-10 sample evinced better corrosion resistance among Mg-BG and Mg-Zn-BG samples due to the presence of Mg_2Si phase that acted as a partial coating. However, the significantly higher corrosion rates observed in immersion tests compared to electrochemical test is due to the variation involved in sample exposure area and duration of tests.

References

1. P. Jeyachandran, S. Bontha, S. Bodhak, V.K. Balla, B. Kundu, and M. Doddamani, Mechanical Behaviour of Additively Manufactured Bioactive Glass/High Density Polyethylene Composites, *J. Mech. Behav. Biomed. Mater*, 2020, **108**, p 103830.
2. S. Bose, S. Vahabzadeh, and A. Bandyopadhyay, Bone Tissue Engineering Using 3D Printing, *Mater. Today*, 2013, **16**(12), p 496–504.
3. N.T. Kirkland, N. Birbilis, and M.P. Staiger, Assessing the Corrosion of Biodegradable Magnesium Implants: A Critical Review of Current Methodologies and Their Limitations, *Acta Biomater.*, 2012, **8**(3), p 925–936.
4. F. Witte, N. Hort, C. Vogt, S. Cohen, K.U. Kainer, R. Willumeit, and F. Feyerabend, Degradable Biomaterials Based on Magnesium Corrosion, *Curr. Opin. Solid State Mater. Sci.*, 2008, **12**(5–6), p 63–72.
5. H. Yoshikawa and, A. Myoui, Bone Tissue Engineering with Porous Hydroxyapatite Ceramics, *J. Artif. Organs*, 2005, **8**(3), p 131–136.
6. F. Witte, F. Feyerabend, P. Maier, J. Fischer, M. Störmer, C. Blawert, W. Dietzel, and N. Hort, Biodegradable Magnesium–Hydroxyapatite Metal Matrix Composites, *Biomaterials*, 2007, **28**(13), p 2163–2174.
7. S. Jaiswal, R.M. Kumar, P. Gupta, M. Kumaraswamy, P. Roy, and D. Lahiri, Mechanical, Corrosion and Biocompatibility Behaviour of Mg-3Zn-HA Biodegradable Composites for Orthopaedic Fixture Accessories, *J. Mech. Behav. Biomed. Mater*, 2018, **78**, p 442–454.
8. Y. Wan, T. Cui, W. Li, C. Li, J. Xiao, Y. Zhu, D. Ji, G. Xiong, and H. Luo, Mechanical and Biological Properties of Bioglass/Magnesium Composites Prepared via Microwave Sintering Route, *Mater. Des.*, 2016, **99**, p 521–527.
9. K. Kowalski, M.U. Jurczyk, P.K. Wirstlein, J. Jakubowicz, and M. Jurczyk, Bioglass Addition on Microstructure and Properties of Ultrafine Grained (Mg-4Y-5.5 Dy-0.5 Zr) Alloy, *Mater. Sci. Eng. B*, 2017, **219**, p 28–36.
10. S. Dutta, K.B. Devi, S. Gupta, B. Kundu, V.K. Balla, and M. Roy, Mechanical and In Vitro Degradation Behavior of Magnesium-Bioactive Glass Composites Prepared by SPS for Biomedical Applications, *J. Biomed. Mater. Res. B Appl. Biomater.*, 2019, **107**(2), p 352–365.
11. S. Dutta, K.B. Devi, S. Mandal, A. Mahato, S. Gupta, B. Kundu, V.K. Balla, and M. Roy, In Vitro corrosion and Cytocompatibility Studies of Hot Press Sintered Magnesium-Bioactive Glass Composite, *Materialia*, 2019, **5**, p 100245.
12. S. Nayak, B. Bhushan, R. Jayaganthan, P. Gopinath, R.D. Agarwal, and D. Lahiri, Strengthening of Mg Based Alloy Through Grain Refinement for Orthopaedic Application, *J. Mech. Behav. Biomed. Mater.*, 2016, **59**, p 57–70.
13. B.P. Zhang, Y. Wang, and L. Geng, Research on Mg-Zn-Ca Alloy as Degradable Biomaterial, *Biomater.—Phys. Chem.*, 2011, p 184–204
14. P. Sekar, S. Narendranath, and V. Desai, Recent Progress in in Vivo Studies and Clinical Applications of Magnesium Based Biodegradable Implants: A Review, *J. Magnes. Alloys*, 2021, **9**(4), p 1147–1163.
15. S. Prithivirajan, S. Narendranath, and V. Desai, Analysing the Combined Effect of Crystallographic Orientation and Grain Refinement on Mechanical Properties and Corrosion Behaviour of ECAPed ZE41 Mg Alloy, *J. Magnes. Alloys*, 2020, **8**(4), p 1128–1143.
16. P. Sekar, N. Sanna, and V. Desai, Enhancement of Resistance to Galvanic Corrosion of ZE41 Mg Alloy by Equal Channel Angular Pressing, *Mater. Corros.*, 2020, **71**(4), p 571–584.
17. H. Duan, C. Cao, X. Wang, J. Tao, C. Li, H. Xin, J. Yang, Y. Song, and F. Ai, Magnesium-Alloy Rods Reinforced Bioglass Bone Cement Composite Scaffolds with Cortical Bone-Matching Mechanical Properties and Excellent Osteoconductivity for Load-Bearing Bone In Vivo Regeneration, *Sci. Rep.*, 2020, **10**(1), p 1–14.
18. E.P.S. Nidadavolu, D. Krüger, B. Zeller-Plumhoff, D. Tolnai, B. Wiese, F. Feyerabend, T. Ebel, and R. Willumeit-Römer, Pore Characterization of PM Mg–0.6 Ca Alloy and its Degradation Behavior Under Physiological Conditions, *J. Magnes. Alloys*, 2020, **9**(2), p 686–703.
19. R. Havaldar, S.C. Pilli, and B.B. Putti, Insights into the Effects of Tensile and Compressive Loadings on Human Femur Bone, *Adv. Biomed. Res.*, 2014, **3**, p 101.

20. M. Knapek, M. Zemková, A. Greš, E. Jablonská, F. Lukáč, R. Král, J. Bohlen, and P. Minárik, Corrosion and Mechanical Properties of a Novel Biomedical WN43 Magnesium Alloy Prepared by Spark Plasma Sintering, *J. Magnes. Alloys*, 2021, **9**(3), p 853–865.

21. D. Dvorský, J. Kubásek, M. Roudnická, F. Průša, D. Nečas, P. Minárik, J. Stráská, and D. Vojtěch, The Effect of Powder Size on the Mechanical and Corrosion Properties and the Ignition Temperature of WE43 Alloy Prepared by Spark Plasma Sintering, *J. Magnes. Alloys*, 2021, **9**(4), p 1349–1362.

22. J. Walker, S. Shadanbaz, N.T. Kirkland, E. Stace, T. Woodfield, M.P. Staiger, and G.J. Dias, Magnesium Alloys: Predicting In Vivo Corrosion with In Vitro Immersion Testing, *J. Biomed. Mater. Res. Part B Appl. Biomater.*, 2012, **100**, p 1134–1141.

23. A.D. King, N. Birbilis, and J.R. Scully, Accurate Electrochemical Measurement of Magnesium Corrosion Rates; A Combined Impedance, Mass-Loss and Hydrogen Collection Study, *Electrochem. Acta*, 2014, **121**, p 394–406.

24. M.C. Zhao, M. Liu, G.L. Song, and A. Atrens, Influence of pH and Chloride Ion Concentration on the Corrosion of Mg Alloy ZE41, *Corros. Sci.*, 2008, **50**(11), p 3168–3178.

25. N. Dinodi and, A.N. Shetty, Alkyl Carboxylates as Efficient and Green Inhibitors of Magnesium Alloy ZE41 Corrosion in Aqueous Salt Solution, *Corros. Sci.*, 2014, **85**, p 411–427.

26. M. Jamesh, S. Kumar, and T.S. Narayanan, Corrosion Behavior of Commercially Pure Mg and ZM21 Mg Alloy in Ringer's Solution–Long Term Evaluation by EIS, *Corros. Sci.*, 2011, **53**(2), p 645–654.

27. D. Mei, S.V. Lamaka, X. Lu, and M.L. Zheludkevich, Selecting Medium for Corrosion Testing of Bioabsorbable Magnesium and Other Metals–A Critical Review, *Corros. Sci.*, 2020, **171**, p 108722.

28. D. Mei, C. Wang, S.V. Lamaka, and M.L. Zheludkevich, Clarifying the Influence of Albumin on the Initial Stages of Magnesium Corrosion in Hank's Balanced Salt Solution, *J. Magnes. Alloys*, 2020, **9**(3), p 805–817.

29. P.N. Lim, R.N. Lam, Y.F. Zheng, and E.S. Thian, Magnesium-Calcium/Hydroxyapatite (Mg-Ca/HA) Composites with Enhanced Bone Differentiation Properties for Orthopedic Applications, *Mater. Lett.*, 2016, **172**, p 193–219.

30. A. Kumar and, P.M. Pandey, Effect of Ultrasonic Assisted Sintering on Mechanical Properties and Degradation Behaviour of Mg15Nb3Zn1Ca Biomaterial, *J. Magnes. Alloys*, 2020 https://doi.org/10.1016/j.jma.2020.11.006

31. M. Kang, Y. Estrin, H. Jung, S. Kim, S. Lee, H. Kim, and Y. Koh, Production and Bio-Corrosion Resistance of Porous Magnesium with Hydroxyapatite Coating for Biomedical Applications, *Mater. Lett.*, 2013, **108**, p 122–124.

32. V.S. Yadav, M.R. Sankar, and L.M. Pandey, Coating of Bioactive Glass on Magnesium Alloys to Improve its Degradation Behavior: Interfacial Aspects, *J. Magnes. Alloys*, 2020, **8**(4), p 999–1015.